



**Universidade Federal do ABC**



**Curso de Pós-Graduação em Nanociências e Materiais Avançados**

**Dissertação de Mestrado**

**Daniel Angel Bellido Aguilar**

**Incorporação de Impurezas pelo Método do Complexo Polimerizado em  
Nanoestruturas de Óxido de Ferro**

**SANTO ANDRÉ**

**2015**





**Universidade Federal do ABC**



**Incorporação de Impurezas pelo Método do Complexo Polimerizado em  
Nanoestruturas de Óxido de Ferro**

**Incorporation of Impurities into Iron Oxide Nanostructures by the Polymerized  
Complex Method**

**Daniel Angel Bellido Aguilar**

**Thesis submitted in partial fulfilment of the  
requirements for the master's degree in  
Nanosciences and Advanced Materials, under  
supervision of Prof. Dr. Flavio Leandro de Souza.**

**Dissertação apresentada como parte dos  
requisitos para obtenção do título de mestre em  
Nanociências e Materiais Avançados, sob  
orientação do Prof. Dr. Flavio Leandro de Souza.**

**SANTO ANDRÉ**

**2015**

**Este exemplar foi revisado e alterado em relação à versão original, de acordo com as observações levantadas pela banca no dia da defesa, sob responsabilidade única do autor e com a anuência de seu orientador.**

**Santo André, \_\_\_\_ de \_\_\_\_\_ de 20\_\_\_\_.**

**Assinatura do autor: \_\_\_\_\_**

**Assinatura do orientador: \_\_\_\_\_**

*“Call to me, and I will answer you, and show you great and mighty things, which  
you know not”.*  
Jeremiah 33:3

### **FINANCIAL SUPPORT**

I am thankful to the scholarship program of OEA-GCUB 2012 which gave me the opportunity to study for my master's degree at the UFABC.

## ACKNOWLEDGEMENTS

I would like to thank my Lord for everything I have. All my strengths come from Him, and to God be the glory.

I would like to thank my parents for their huge love and great teachings. They always encouraged me to fly high.

I would like to thank all those unknown and known persons who supported my graduated and postgraduate studies.

I would like to thank professor Flavio for providing me with all the tools to finish my master's degree successfully.

I would like to thank all my friends of the Laboratory of Alternative Energy and Nanomaterials (LEAN) for helping me since the beginning of my master's degree, specially, Waldemir, André, Vinicius, Fernanda and Nathalie.

I would like to thank Prof. Carlos José L. Constantino and Dr. Leonardo N. Furini for the Raman spectra of the hematite films obtained in UNESP-Presidente Prudente.

I would like to thank the research group of Prof. Dr. Edson Leite for the SEM images obtained in the *Laboratório de Nanocaracterização* in UFSCAR.

## ABSTRACT

Iron oxide is one of the most promising semiconductors for applications as photoanodes in photoelectrochemical cells. A simple and cheap route to prepare hematite photoelectrodes is the sol-gel method. Hematite thin films can be also prepared by using the polymerized complex (PC) method that is a sol-gel method derived technique. This methodology involves the formation of complexes of metal ions that then undergo polymerization. In addition, the PC method allows an optimal control of stoichiometry and of the incorporation of impurities during the process. In this work, pure and doped hematite thin films were prepared by using the PC method at two different heat treatments (500°C and 800°C). The  $\alpha\text{-Fe}_2\text{O}_3$  thin films were modified with two differently charged dopants ( $\text{Zn}^{2+}$  and  $\text{Sn}^{4+}$ ), and their photoelectrochemical properties were studied in comparison with the pure hematite films. Hematite electrodes prepared at 800°C exhibited the best photocatalytic response in comparison with 500°C-treated hematite films. This effect was attributed to the higher roughness and surface area of films synthesized at higher temperatures. Furthermore, the modification of  $\alpha\text{-Fe}_2\text{O}_3$  with  $\text{Zn}^{2+}$  and  $\text{Sn}^{4+}$  ions resulted in a better photoresponse and stability as showed by the linear sweep voltammetry and chronoamperometry results. Dopants influenced differently on the photocurrent onset potential and the potential for the electrocatalytic oxygen evolution. In addition, results suggested that impurities were incorporated more efficiently into the hematite films prepared at 800°C. Nevertheless, the photocatalytic properties of the undoped and modified hematite films was poor, and two plausible hypothesis are proposed to explain the poor performance of hematite electrodes. First, most of dopants may have segregated, and, according to the previous reports in the literature, they may have acted as recombination sites that reduced the efficiency of the charge separation (photogenerated electron-hole pair). Second, poor contact between the hematite and F-SnO<sub>2</sub> layer (from substrate) may have formed that severely hindered the harvesting of the photogenerated charges. The overall consequence of these two effects is the reduction in the activity of hematite films under illumination conditions.

**Key words:** iron oxide, nanostructure, thin film, doping.



## RESUMO

O óxido de ferro é um dos semicondutores mais promissores para aplicações como fotoânodos em células fotoeletroquímicas. Uma rota simples e barata para preparar fotoeletrodos de hematita é o método sol-gel. Filmes finos de hematita podem também ser preparados utilizando o método do complexo polimerizado (CP) que é um método derivado da técnica sol-gel. Esta metodologia envolve a formação de complexos de íons metálicos que em seguida se polimerizam. Além disso, o método do CP permite um controle ótimo da estequiometria e da incorporação de impurezas durante o processo. Neste trabalho, filmes finos de hematita pura e dopada foram preparados utilizando o método do CP em dois tratamentos térmicos diferentes (500°C e 800°C). Os filmes finos de  $\alpha\text{-Fe}_2\text{O}_3$  foram modificados com dois dopantes de cargas diferentes ( $\text{Zn}^{2+}$  e  $\text{Sn}^{4+}$ ) e as suas propriedades fotoeletroquímicas foram estudadas em comparação com os filmes de hematita pura. Os eletrodos de hematita preparados a 800°C apresentaram a melhor resposta fotocatalítica em comparação com os filmes de hematita preparados a 500°C. Este efeito foi atribuído à maior rugosidade e área superficial dos filmes sintetizados a temperaturas mais elevadas. Além disso, a modificação de  $\alpha\text{-Fe}_2\text{O}_3$  com os íons  $\text{Zn}^{2+}$  e  $\text{Sn}^{4+}$  resultou em uma melhor fotoresposta e estabilidade como demonstrado pelos resultados da voltametria linear e cronoamperometria. Os dopantes influenciaram de forma diferente no potencial do começo da fotocorrente e no potencial da evolução de oxigênio eletrocatalítica. Além disso, os resultados sugeriram que as impurezas foram incorporadas de forma mais eficiente nos filmes de hematita preparados a 800°C. Porém, as propriedades fotocatalíticas dos filmes de hematita não dopada e modificada não foram significativas, e duas hipóteses plausíveis são propostas para explicar o baixo desempenho dos eletrodos de hematita. Em primeiro lugar, a maioria dos dopantes podem ter segregado, e, de acordo com o reportado na literatura, eles podem estar atuando como sítios de recombinação que reduziram a eficiência da separação das cargas (par elétron-buraco fotogerado). Em segundo lugar, mau contato entre a camada de hematita e  $\text{F-SnO}_2$  (do substrato) pode ter sido formado que impediu severamente a colheita das cargas fotogeradas. A consequência global destes dois efeitos é a redução da atividade fotocatalítica dos filmes de hematita.

**Palavras chaves:** óxido de ferro, nanoestruturas, filmes finos, dopagem.

## FIGURES

FIGURE 1. GLOBAL ENERGY CONSUMPTION BY TYPE OF ENERGY SOURCE FROM 1971 TO 2011 <sup>2</sup> .....	1
FIGURE 2. WORLD TOTAL ENERGY SUPPLY BY TYPE OF ENERGY SOURCE IN 2011 <sup>2</sup> .....	2
FIGURE 3. (A) ELECTRON ENERGY LEVELS IN A METAL, AN INTRINSIC SEMICONDUCTOR AND A REDOX PAIR. $E_{\text{RED}}$ = REDUCTANT PARTICLE, $E_{\text{OX}}$ = OXIDANT PARTICLE. ENERGY DIAGRAM FOR A SEMICONDUCTOR AND REDOX PAIR BEFORE (B) EQUILIBRIUM AND (C) IN EQUILIBRIUM. ADAPTED FROM SATO <sup>10</sup> . ....	5
FIGURE 4. (A) CHARGE TRANSPORT IN THE ABSORPTION REGIONS OF A SEMICONDUCTOR. $L_D$ =DIFFUSION LENGTH, $W$ =DEPLETION LAYER WIDTH. THE EFFECT OF APPLYING AN EXTERNAL POTENTIAL ON A SEMICONDUCTOR BY USING (B) A LOW POTENTIAL AND (C) A HIGH POTENTIAL.....	7
FIGURE 5. BAND EDGE POSITIONS FOR VARIOUS SEMICONDUCTORS IN RELATION TO VARIOUS REDOX POTENTIALS <sup>15</sup> . ....	9
FIGURE 6. PEC CONFIGURATIONS: A) S2 PEC AND B) D4 PEC.....	10
FIGURE 7. ENERGY DIAGRAMS OF A S2 PHOTOELECTROCHEMICAL CELL. THE N-TYPE SEMICONDUCTOR AND THE METAL ACT AS THE ANODE AND THE CATHODE, RESPECTIVELY. A) OPEN CIRCUIT IN DARKNESS. B) CLOSED CIRCUIT IN DARKNESS. (C) CLOSED CIRCUIT UNDER ILLUMINATION CONDITIONS IN WHICH THE WATER SPLITTING IS POSSIBLE. ADAPTED FROM SATO <sup>10</sup> .....	11
FIGURE 8. POINT DEFECT REPRESENTATION USING THE KRÖGER-VINK NOTATION. ADAPTED FROM VAN DE KROL AND GRATZEL <sup>13</sup> . ....	13
FIGURE 9. POINT DEFECT LEVELS OF CU-DOPED ZNO CAUSING DIFFERENT PHOTOLUMINESCENCE TRANSITIONS <sup>21</sup> . ....	15
FIGURE 10. HEXAGONAL UNIT CELL OF $\alpha\text{-Fe}_2\text{O}_3$ . RED AND BLUE SPHERES REPRESENT OXYGEN AND IRON ATOMS, RESPECTIVELY <sup>25</sup> . ....	16
FIGURE 11. PECHINI METHOD SEQUENCE FOR THE PREPARATION OF METAL OXIDES.....	18
FIGURE 12. XRD PATTERNS OF HEMATITE FILMS PREPARED BY THE POLYMERIZED COMPLEX METHOD WITH ADDITIONAL THERMAL TREATMENT AT DIFFERENT TEMPERATURES FOR (A) UNDOPED HEMATITE FILMS, (B) SN-MODIFIED HEMATITE FILMS AND (C) ZN-MODIFIED HEMATITE FILMS. DIFFRACTION PEAKS OF THE $\text{F-SnO}_2$ ARE INDICATED WITH ASTERISKS. ....	23
FIGURE 13. RAMAN SPECTRA: A) FILMS PREPARED AT 500°C, B) FILMS PREPARED AT 800°C. WELL-DEFINED BANDS ARE INDICATED WITH ASTERISKS. ....	27
FIGURE 14. TOP-VIEW MICROGRAPHS OF HEMATITE FILMS: (A) $\alpha\text{-Fe}_2\text{O}_3$ (500°C), (B) $\alpha\text{-Fe}_2\text{O}_3$ (800°C), (C) $\alpha\text{-Fe}_2\text{O}_3 + \text{Sn}^{4+}$ (500°C), (D) $\alpha\text{-Fe}_2\text{O}_3 + \text{Sn}^{4+}$ (800°C), (E) $\alpha\text{-Fe}_2\text{O}_3 + \text{Zn}^{2+}$ (500°C) F) $\alpha\text{-Fe}_2\text{O}_3 + \text{Zn}^{2+}$ (800°C). CROSS-SECTION IMAGES OF THE UNDOPED FILMS PREPARED AT (G) 500°C AND (H) 800°C.....	30
FIGURE 15. ABSORPTION COEFFICIENT AS FUNCTION OF WAVELENGTH OF HEMATITE FILMS TREATED AT (A) 500°C AND (B) 800°C: ----- $\alpha\text{-Fe}_2\text{O}_3$ , ----- $\alpha\text{-Fe}_2\text{O}_3 + \text{Sn}^{4+}$ , ----- $\alpha\text{-Fe}_2\text{O}_3 + \text{Zn}^{2+}$ . INSET GRAPHS SHOW THE TRANSMITTANCE SPECTRUM OF THE FTO SUBSTRATE. ....	33
FIGURE 16. CALCULATION OF THE DIRECT ELECTRONIC TRANSITION OF ELECTRODES PREPARED AT (A) 500°C AND (B) 800°C. CALCULATION OF THE INDIRECT ELECTRONIC TRANSITION OF HEMATITE ELECTRODES PREPARED AT (C) 500°C AND (D) 800°C.....	34
FIGURE 17. LINEAR SWEEP VOLTAMMOGRAMS: (A) $\alpha\text{-Fe}_2\text{O}_3$ (500°C), (B) $\alpha\text{-Fe}_2\text{O}_3$ (800°C), (C) $\alpha\text{-Fe}_2\text{O}_3 + \text{Sn}^{4+}$ (500°C), (D) $\alpha\text{-Fe}_2\text{O}_3 + \text{Sn}^{4+}$ (800°C), (E) $\alpha\text{-Fe}_2\text{O}_3 + \text{Zn}^{2+}$ (500°C), AND (F) $\alpha\text{-Fe}_2\text{O}_3 + \text{Zn}^{2+}$ (800°C). ....	36

FIGURE 18. PHOTOCHRONOAMPEROGRAMS OF UNDOPED AND MODIFIED HEMATITE FILMS AT 1.23 $V_{RHE}$ . THE PERCENT VARIATION OF THE PHOTOCURRENT IS SHOWN IN RED BRACKETS .....	38
FIGURE 19. MOTT-SCHOTTKY PLOTS OF HEMATITE FILMS PREPARED (A) AT 500°C AND (B) AT 800°C.....	40
FIGURE 20. IMAGES SHOWING THE CONTACT ANGLE FORMED BETWEEN A DROP WATER AND THE HEMATITE FILM SURFACE: A) A- $Fe_2O_3$ (500°C), B) A- $Fe_2O_3 + Sn^{4+}$ (500°C), C) A- $Fe_2O_3 + Zn^{2+}$ (500°C), D) A- $Fe_2O_3$ (800°C), E) A- $Fe_2O_3 + Sn^{4+}$ (800°C) AND F) A- $Fe_2O_3 + Zn^{2+}$ (800°C).....	43
FIGURE 21. AFM MICROGRAPHS: A) A- $Fe_2O_3$ (500°C), B) A- $Fe_2O_3 + Sn^{4+}$ (500°C), C) A- $Fe_2O_3 + Zn^{2+}$ (500°C), D) A- $Fe_2O_3$ (800°C), E) A- $Fe_2O_3 + Sn^{4+}$ (800°C) AND F) A- $Fe_2O_3 + Zn^{2+}$ (800°C).....	45
FIGURE 22 SCHEMATIC REPRESENTATION OF CROSS-SECTION STEM IMAGES SHOWING THAT THE HEMATITE FILMS PREPARED BY THE PC METHOD DID NOT COMPLETELY ADHERE TO F- $SnO_2$ SURFACE. ADAPTED FROM REF. 84. ....	49

## TABLES

TABLE 1. LOWER HEATING VALUES OF COMMON FUELS <sup>5</sup> .....	3
TABLE 2. LATTICE PARAMETERS, CELL VOLUME, ORIENTATION DEGREE AND HEMATITE CRYSTAL SIZE FOR UNDOPED AND MODIFIED HEMATITE FILMS OBTAINED FROM XDR ANALYSIS. HEMATITE STANDARD POWDER DATA WAS ALSO INCLUDED AS REFERENCE. ....	24
TABLE 3. CHARACTER TABLE OF THE POINT GROUP $D_{3D}$ . ....	28
TABLE 4. ESTIMATED DIRECT AND INDIRECT ELECTRONIC TRANSITIONS OF ALL THE SYNTHESIZED HEMATITE FILMS. ....	34
TABLE 5. PHOTOCURRENT DENSITY, $J$ , AT 1.23 $V_{RHE}$ OF HEMATITE ELECTRODES.....	37
TABLE 6. ELECTRONIC PARAMETERS ESTIMATED FROM MOTT-SCHOTTKY CURVES.....	41
TABLE 7. ROUGHNESS VALUES AND AVERAGE CONTACT ANGLES FOR HEMATITE FILMS. ....	44

## SUMMARY

<b>1. INTRODUCTION</b>	1
1.1 Renewable energy sources	1
1.2 Semiconductor-electrolyte interface	3
1.3 Photoelectrochemical cells (PEC) for solar hydrogen production	6
1.4 Point defects and doping of metal oxide semiconductors	12
1.5 Iron oxide (hematite) as photoanode	15
1.6 Polymerized Complex Method	16
<b>2. ADVANCES IN POLYMERIZED COMPLEX METHOD BY LEAN</b>	19
<b>3. OBJECTIVES</b>	20
3.1 General	20
3.2 Specific	20
<b>4. EXPERIMENTAL PROCEDURE</b>	20
4.1 Preparation of undoped and modified iron oxide films	20
4.2 Characterization	21
<b>5. RESULTS</b>	22
5.1 Structural study	22
5.2 Raman spectroscopy	26
5.3 Morphological study	29
5.4 Optical study	31
5.5 Photoelectrochemical study	35
5.6 Electrochemical impedance (EIS)	39
5.7 Surface study	42
<b>6. GENERAL DISCUSSION</b>	46
<b>7. CONCLUSIONS</b>	49
<b>8. SUGGESTIONS FOR FUTURE WORK</b>	50
<b>9. REFERENCES</b>	51

## 1. INTRODUCTION

### 1.1 Renewable energy sources

Energy has always had an important role in the human development through the centuries. However, the world is facing a huge problem related with the energy sources used. Over the last 40 years, fossil fuels have been the major energy source used by humanity (Figure 1). In fact, in 2011, 80% of energy sources came from fossil fuels (Figure 2). The continuing use of this kind of energy brings two important problems. The most serious problem is that combustion of fossil fuel provokes the emission of greenhouse gases such as carbon dioxide<sup>1</sup>. The second problem is that, in the long run, fossil fuels are limited sources and not renewable.

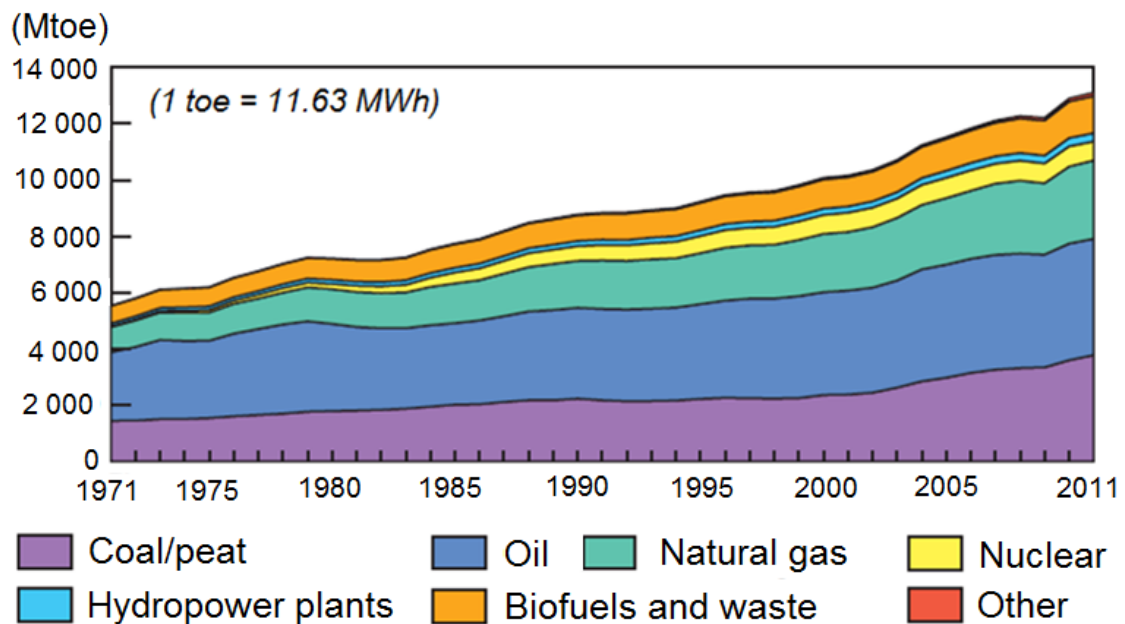


**Figure 1.** Global energy consumption by type of energy source from 1971 to 2011<sup>2</sup>.

Because of the increasing world population, the energy consumption is also increasing (Figure 1). This implies higher consumption of fossil fuels and significant impairment in quality of life due to global warming. Therefore, renewable and clean energy sources are an urgent need for the maintenance of the environment and the population's quality of life.

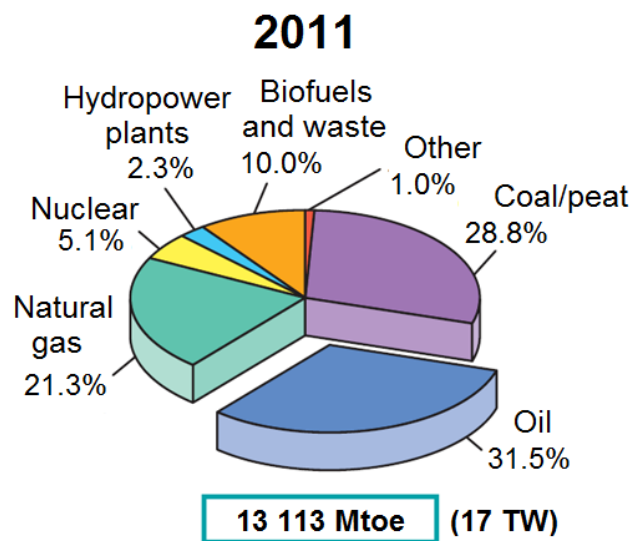


**Figure 2.** World total energy supply by type of energy source in 2011<sup>2</sup>.

Geothermal, nuclear, wind, hydro, biomass and solar energy are the main sustainable energy sources. Each of them has its own advantages and disadvantages. For example, nuclear energy is certainly a mature technology, but it still faces the waste disposal problems and may cause major accidents as those happened in Fukushima (Japan). Hydropower, on the other hand, needs a lot of money for the construction of dams which cause ecological and geological damages. In regard with geothermal energy, usually the available energy is found in great depths from the surface, and the plants have a limited life time (requiring that new areas are perforated). Wind energy is a free source of energy, but it cannot meet the global energy demand. Among the energy sources mentioned above, solar energy stands out because it is a safe, clean and unlimited source which can supply the whole current global energy demand<sup>3</sup>.

Solar energy, however, is intermittent, which means that it is available depending on the geographic location, time of the day and season. One way to overcome those adversities of solar irradiation is to store that energy in the form of chemical energy, that is, in the form of a fuel such as the hydrogen gas.

Hydrogen is an ideal fuel because it is an abundant element and exists both in the water and in the biomass. In addition, it can produce a high energy density when compared with other fossil fuels (Table 1). Additionally, the only product of hydrogen combustion is water that can be recycled to produce new hydrogen with solar energy<sup>3; 4</sup>.

**Table 1.** Lower heating values of common fuels<sup>5</sup>.

	Hydrogen	Petroleum	Methanol	Methane	Propane	Ammonia
<b>Lower heating value<sup>1</sup> (MJ kg<sup>-1</sup>)</b>	120.0	44.38	20.1	50.0	46.4	18.6

Currently, most hydrogen production comes from fossil fuels. Approximately 48% of the production comes from steam methane reforming, 30% from refinery off-gases, 18% from coal gasification and only 4% of hydrogen production from the electrolysis of water. Nevertheless, the hydrogen production by electrolysis of water does not use fully environment-friendly technologies<sup>6; 7</sup>.

Consequently, the production of hydrogen by water splitting by using solar energy is one of the best strategies to solve the world energy problem: this approach makes use of an unlimited and clean source like the sun to produce a high-energy fuel such as hydrogen, and it uses water as the source and generates water as the only product.

There are several processes for hydrogen production by means of solar energy such as: electrolysis, photoelectrolysis, biophotolysis, thermolysis and thermochemical cycles<sup>8</sup>. This study aims to develop nanostructured iron oxide films for use in photoelectrochemical cells.

## 1.2 Semiconductor-electrolyte interface

One of the most important aspects of a photoelectrochemical cell is the semiconductor-electrolyte interface. Both the semiconductor-electrolyte interface and the photoelectrochemical cell operation can be explained by using the concept of electrochemical potential. In general, the electrochemical potential is the energy state of a charged particles system like electrons in a semiconductor, metal and redox pairs. The electrochemical potential is defined as follows<sup>9; 10</sup>:

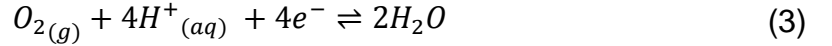
<sup>1</sup> The lower heating value of a fuel is the amount of heat released when the produced gases (carbon dioxide and steam) are cooled to the boiling point of water (100°C).



$$\mu_e = \left( \frac{\partial G}{\partial n_e} \right)_{P,T,n,\varphi} \quad (1)$$

where  $G$  is the Gibbs free energy,  $n_e$  is the electron concentration;  $P$ ,  $T$ ,  $\varphi$  are the pressure, temperature and the inner potential, respectively.

In the water splitting reaction by electrochemical cells, hydrogen is generated at the cathode surface (reduction reaction) while oxygen is produced at the anode surface (oxidation reaction). Therefore, the water-splitting global reaction can be seen as two semireactions:



Each semireaction is a redox pair in which an electron (or hole) is involved. The energy of these redox electrons is defined by their electrochemical potential as defined in Equation 1<sup>10</sup>. Because electrons in a solid phase (such as semiconductor and metal) also take part in the photolysis of water, it is then important to consider their electrochemical potential.

In the case of metals, the Fermi Level and the electrochemical potential are equal at  $T=0$ . However, at  $T \neq 0$  the Fermi level and the electrochemical potential are slightly different so that, for experimental purposes, they are considered equal. This approximation is also applied for semiconductors<sup>11</sup>. In addition, we can define a Fermi level of a redox pair as a synonym of its electrochemical potential.

When dealing with a system of a pure phase containing only one kind of charged particles such as electrons, the electrochemical potential reduces to:

$$\mu_e = \frac{G}{N} = E_F \quad (4)$$

where  $N$  is the number of electrons in the system. Figure 3a shows the energy diagrams of electrons in a metal, semiconductor and redox pair.

When a semiconductor is immersed in a solution containing a redox pair, the Fermi levels of the semiconductor and the redox pair are different in the solid-liquid interface. However, both Fermi levels reach equilibrium due to the flow of charge

between the phases. The Fermi level equilibrium for an N-Type semiconductor is shown in Figure 3b. In this case, the electrons migrate to the interface and cause that the semiconductor donor impurities become positively ionized. Because of the missing electrons in the region of the ionized donors, a depletion layer is originated whose width is given by  $W$ . In addition, the charge separation creates an internal electric field which makes the energy bands be represented as bended in the surface. The direction of the electric field allows positive charges to be directed to the solid-liquid interface and negative charges to be conducted to the external circuit. The depletion layer is also created when a semiconductor and metal are in contact<sup>12</sup>.

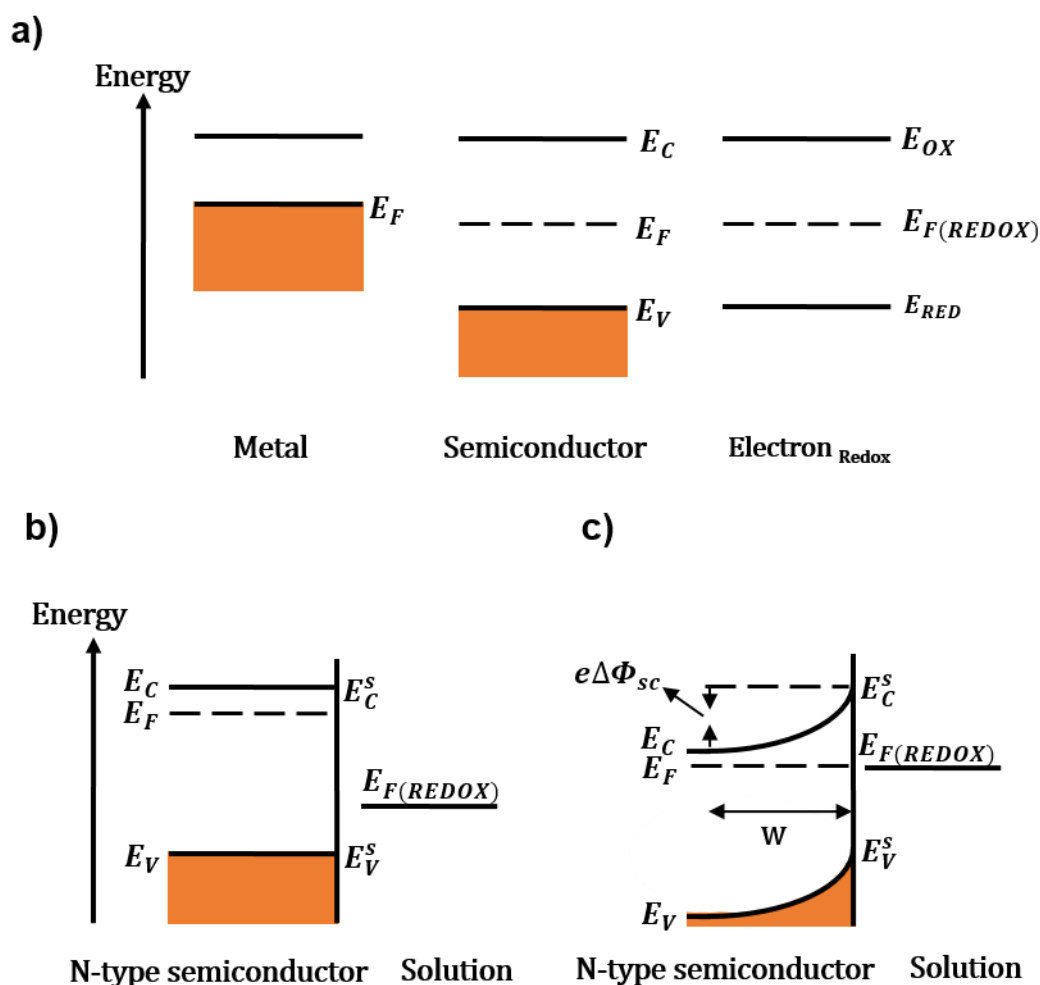


**Figure 3.** (a) Electron energy levels in a metal, an intrinsic semiconductor and a redox pair.  $E_{red}$ = Reductant particle,  $E_{ox}$ = Oxidant particle. Energy diagram for a semiconductor and redox pair before (b) equilibrium and (c) in equilibrium. Adapted from Sato<sup>10</sup>.

Electron-hole pairs are generated when a semiconductor is illuminated by a wavelength with energy greater than its band gap energy. Not all photogenerated electron-hole pairs will contribute to the photocurrent. The electron-hole pairs will recombine or not, and it will depend on the region where they are generated. Assuming the incidence of light through the electrolyte, in Figure 4a is shown three absorption regions for an N-type semiconductor. As mentioned above, the first region is the depletion layer which allows the separation of the photogenerated charges which, therefore, contribute to the measured photocurrent. The second region is defined by the hole-diffusion length. The holes photogenerated in this region can reach the depletion layer before recombining and thus contribute to the photocurrent. Within the third region (the region beyond the  $L_D + W$  layer), the electron-hole pairs recombine because there is no electric field and the diffusion process is not effective<sup>13</sup>.

Another important aspect in the semiconductor-electrolyte interface is the application of an external potential. For the evaluation of the photoelectrochemical properties, an external potential (relative to a reference potential) is applied to the semiconductor electrode. This potential is distributed over the depletion layer and the Helmholtz layer<sup>2</sup> which both act as two capacitors in series:

$$\frac{1}{C_{total}} = \frac{1}{C_{sc}} + \frac{1}{C_H} \quad (5)$$

because  $C_H \gg C_{sc}$ , the application of an external potential is distributed mainly on the semiconductor layer. Therefore, the application of a potential on the semiconductor allows varying the thickness and capacitance of the depletion layer<sup>12</sup>; <sup>13</sup> (Figure 4b).

### 1.3 Photoelectrochemical cells (PEC) for solar hydrogen production

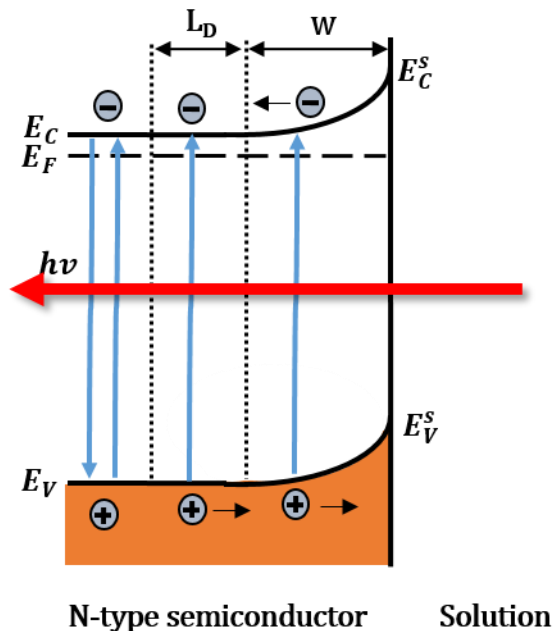
The photolysis of water is done in a photoelectrochemical cell which has two semiconductor electrodes or a metal electrode and a semiconductor electrode. For its operation, the semiconductor (s) must be illuminated by a light source with energy

---

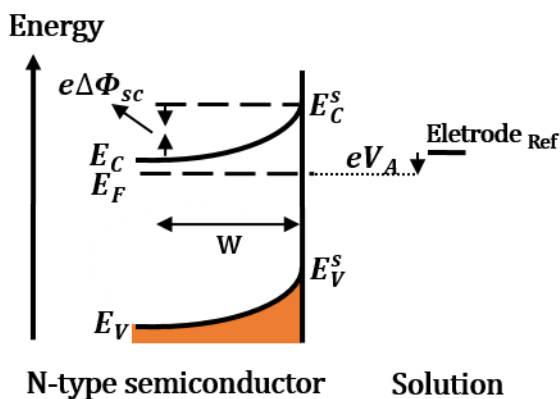
<sup>2</sup> The Helmholtz layer is made up of two layers: the inner layer composed of adsorbed solvent molecules and ions at the electrode surface; the outer layer composed of solvated ions.

greater than its band-gap energy in order to generate electron-hole pairs which then induce the reduction and oxidation processes.

a)



b)



c)

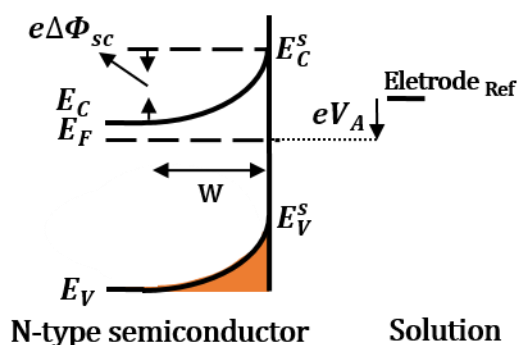


**Figure 4.** (a) Charge transport in the absorption regions of a semiconductor.  $L_D$ =diffusion length,  $W$ =depletion layer width. The effect of applying an external potential on a semiconductor by using (b) a low potential and (c) a high potential.

When a semiconductor is illuminated (photostationary state), the concentration of electrons and hole changes. Therefore, one can define an individual Fermi level for electrons and holes in the photostationary state. Since thermal equilibrium is not achieved between the photogenerated electrons and holes, this individual Fermi level is called the quasi Fermi level<sup>12</sup>. The quasi Fermi level is considered as the driving force for charge-transfer reactions.

Thus, the transfer of electrons from the conduction band to oxidant particles is only possible if the following condition is fulfilled:

$$E_{F,n} > E_{F(REDOX)} \quad (6)$$

Likewise, the transfer of hole from valence band to reductant particles is possible when:

$$E_{F,p} < E_{F(REDOX)} \quad (7)$$

In relation with the above inequations, the thermodynamic condition for electrolysis of water is:

$$E_{F,n} > E_{F(H^+/H_2)} \quad (8)$$

$$E_{F,p} < E_{F(O_2/H_2O)} \quad (9)$$

These conditions will be met depending on the conduction and valence band edge positions of the semiconductor relative to the reduction and oxidation potentials of water. Therefore, the main requirement for water splitting is that the band edge positions of the semiconductor must straddle the reduction and oxidation potentials of water.

A PEC composed of a single semiconductor (such as  $\text{SrTiO}_3$ ) and metal counter electrode is denominated a S2 PEC<sup>3</sup>. However, not all the semiconductors are capable of splitting water themselves because of their band edge positions (Figure 5). For example,  $\text{Fe}_2\text{O}_3$ ,  $\text{WO}_3$  and  $\text{SnO}_2$  electrodes cannot meet the conditions described in Equations 8 and 9. Nevertheless, those type of semiconductors can be used in pairs (a photoanode and photocathode) to solve the problem of band edge positions. This PEC configuration is called D4<sup>4</sup>, and the photoanode and photocathode can be made of a single semiconductor or two different semiconductors. Figure 6 compares the two main PEC configurations.

---

<sup>3</sup> "S" stands for a single semiconductor and "2" means that the semiconductor has to absorb two photons to produce one molecule of  $\text{H}_2$ .

<sup>4</sup> Here "D" stands for dual semiconductors and "4" means that four photons are required to produce one molecule of  $\text{H}_2$ .

The following paragraphs explain the work operation of a S2 PEC; the same reasoning can be applied for a D4 PEC.

When the semiconductor and metal electrodes are not connected in the dark, their Fermi levels are not in equilibrium as shown in Figure 7a for an N-type semiconductor. Nevertheless, both Fermi levels achieve equilibrium when both electrodes are connected and maintained in darkness (Figure 7b)<sup>14</sup>. Furthermore, in this condition the depletion layer is formed and its potential is denoted by  $\Delta\Phi_{SC}$

13.

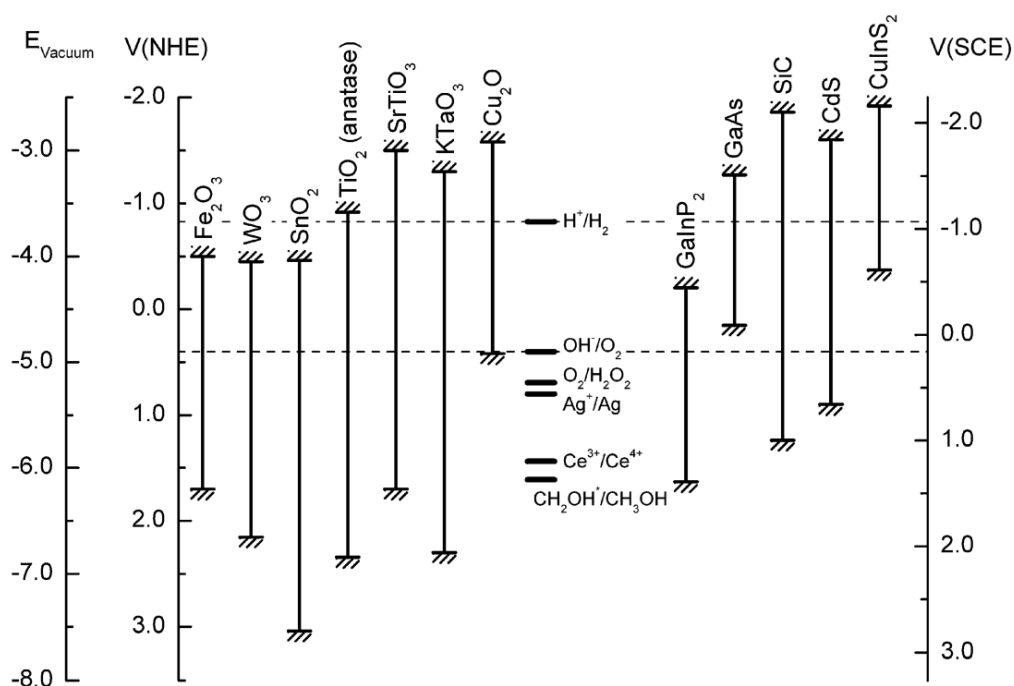


**Figure 5.** Band edge positions for various semiconductors in relation to various redox potentials<sup>15</sup>.

In the absence of light, it is not thermodynamically possible to observe the oxygen evolution at the semiconductor surface because its Fermi level is located upper than  $E_{F(O_2/H_2O)}$ . In addition, the N-type semiconductor possesses a low hole concentration which makes the charge-transfer reaction less favorable to occur. Likewise, hydrogen reduction is not possible at the metal cathode because the Fermi level of the metal is lower than the  $E_{F(H^+/H_2)}$ .

On the contrary, when an N-type semiconductor is illuminated its Fermi level raises an energy equivalent to its photopotential (Figure 7c). The photopotential is a potential originated by the migration of the photogenerated electrons and holes,

which decreases the potential of the depletion layer. Since the metal cathode is short-circuited with the semiconductor, the Fermi level of the metal also rises the same energy equivalent to the photopotential, so that, it is higher than the  $E_{F(H^+/H_2)}$ . This condition makes the electron transfer possible for the hydrogen reduction at metal surface. Moreover, the hole concentration increases at the anode surface that causes the Fermi level of holes to be lower than  $E_{F(O_2/H_2O)}$ ; this means that the hole transfer for oxygen evolution is thermodynamically possible. The global reaction is, therefore, the water splitting in which hydrogen gas is produced at the semiconductor anode and oxygen gas is generated at the metal cathode<sup>10; 16; 17</sup>.

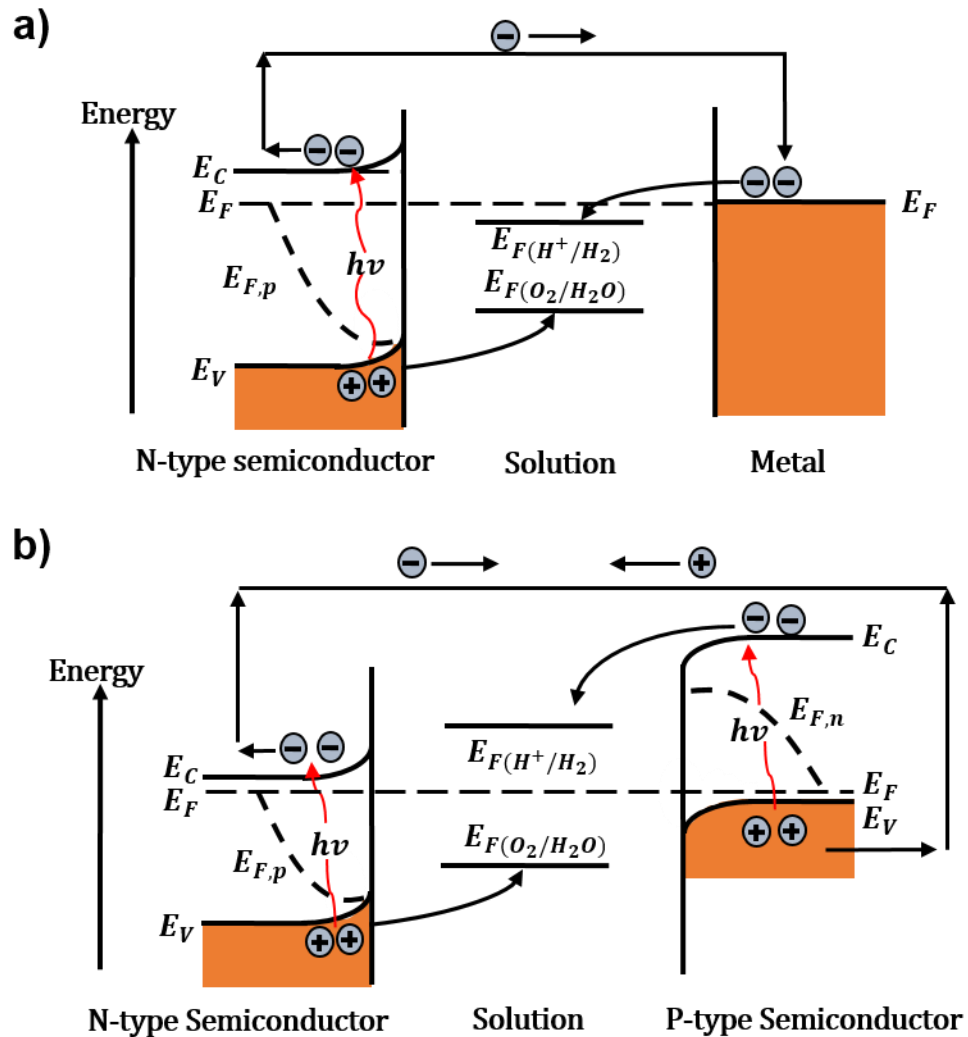


**Figure 6.** PEC configurations: a) S2 PEC and b) D4 PEC.

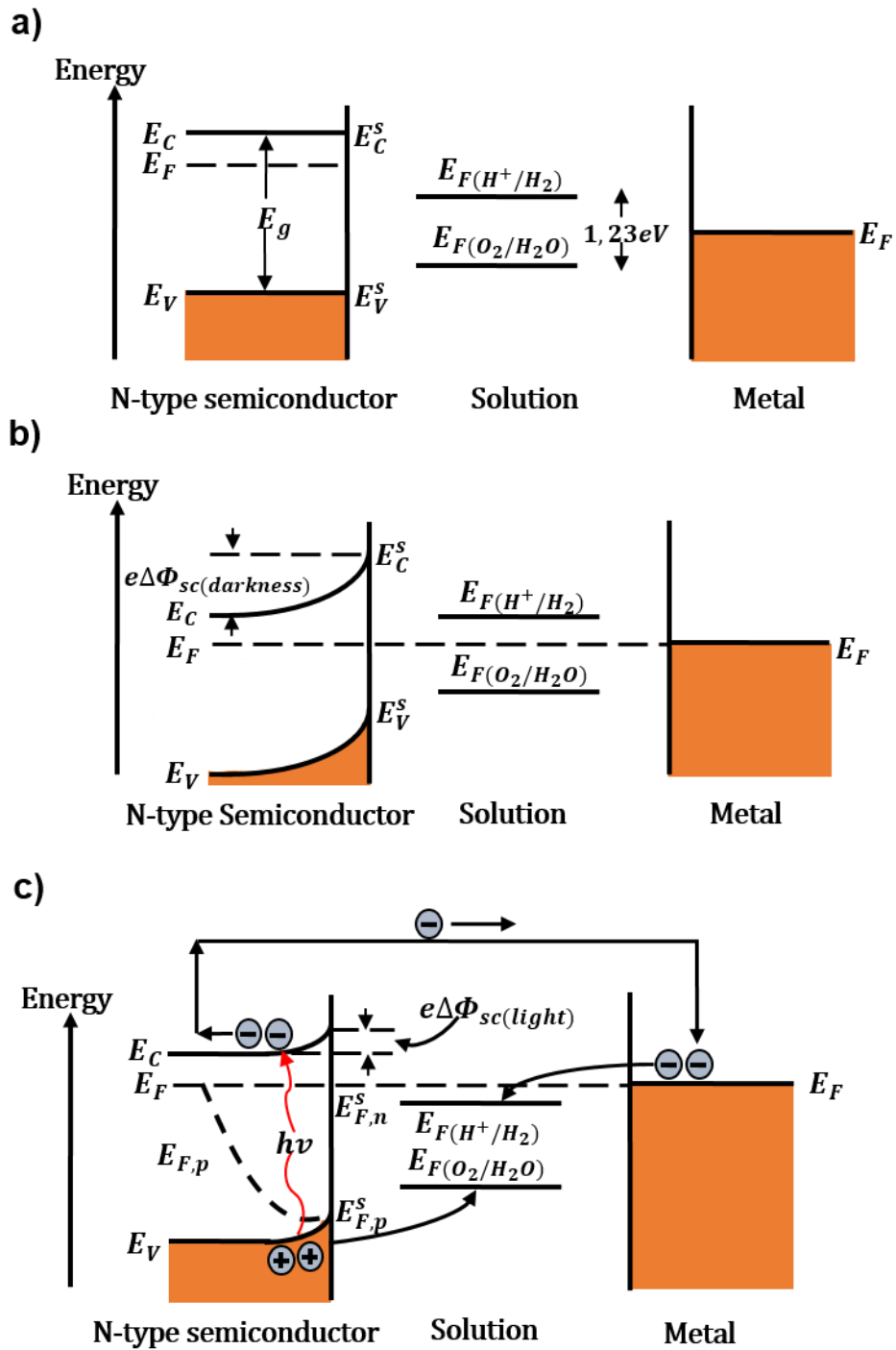


**Figure 7.** Energy diagrams of a S2 photoelectrochemical cell. The N-type semiconductor and the metal act as the anode and the cathode, respectively. a) Open circuit in darkness. b) Closed circuit in darkness. (c) Closed circuit under illumination conditions in which the water splitting is possible. Adapted from Sato<sup>10</sup>.



The performance of a photoanode or photocathode not only depends on its conduction and valence band edge positions but also other important features such as<sup>13</sup>:

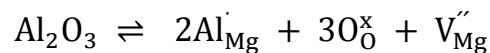
- Good visible-region absorption
- Chemical stability in dark and light conditions
- Efficient charge transport
- Low reduction and oxidation overpotentials

#### 1.4 Point defects and doping of metal oxide semiconductors

In the ceramic context, point defects are basically classified into four categories: vacancies, interstitials, substitutional (impurities) and electronic defects. Electron-hole pairs thermally generated are regarded as electronic defects when compared with the electronic ground state at 0 K. In general, the creation of point defects in ionic materials is described as a chemical reaction. These defect reactions are written by using the Kröger-Vink notation (Figure 8). Furthermore, defect reaction equations must fulfill three important rules: a) mass conservation, b) charge conservation and c) site conservation.

The first two rules mean that any defect reaction cannot lead to a gain or loss of mass and charge, respectively. Site conservation refers to the conservation of the proportion of the cation sites to the anion sites<sup>18</sup>. Some examples are given for illustrating these rules:

a) Formation of a dilute solution of  $\text{Al}_2\text{O}_3$  in  $\text{MgO}$ :



In this reaction, neither aluminum nor oxygen atoms are created when doping  $\text{MgO}$  with  $\text{Al}_2\text{O}_3$ , therefore, the mass conservation rule is satisfied. Moreover, this equation is charge balanced because the charge of two Al substitutionals is compensated by the charge of one Mg vacancy (charge conservation). The stoichiometry ratio of cation site to anion site is 1:1 for the  $\text{MgO}$ , and, after doping with  $\text{Al}_2\text{O}_3$ , that relation is conserved: there are three anion positions ( $\text{O}_0^{\times}$ ) and three cation positions (two  $\text{Al}_{\text{Mg}}^{\cdot}$  and one  $\text{V}_{\text{Mg}}^{\prime\prime}$ ).

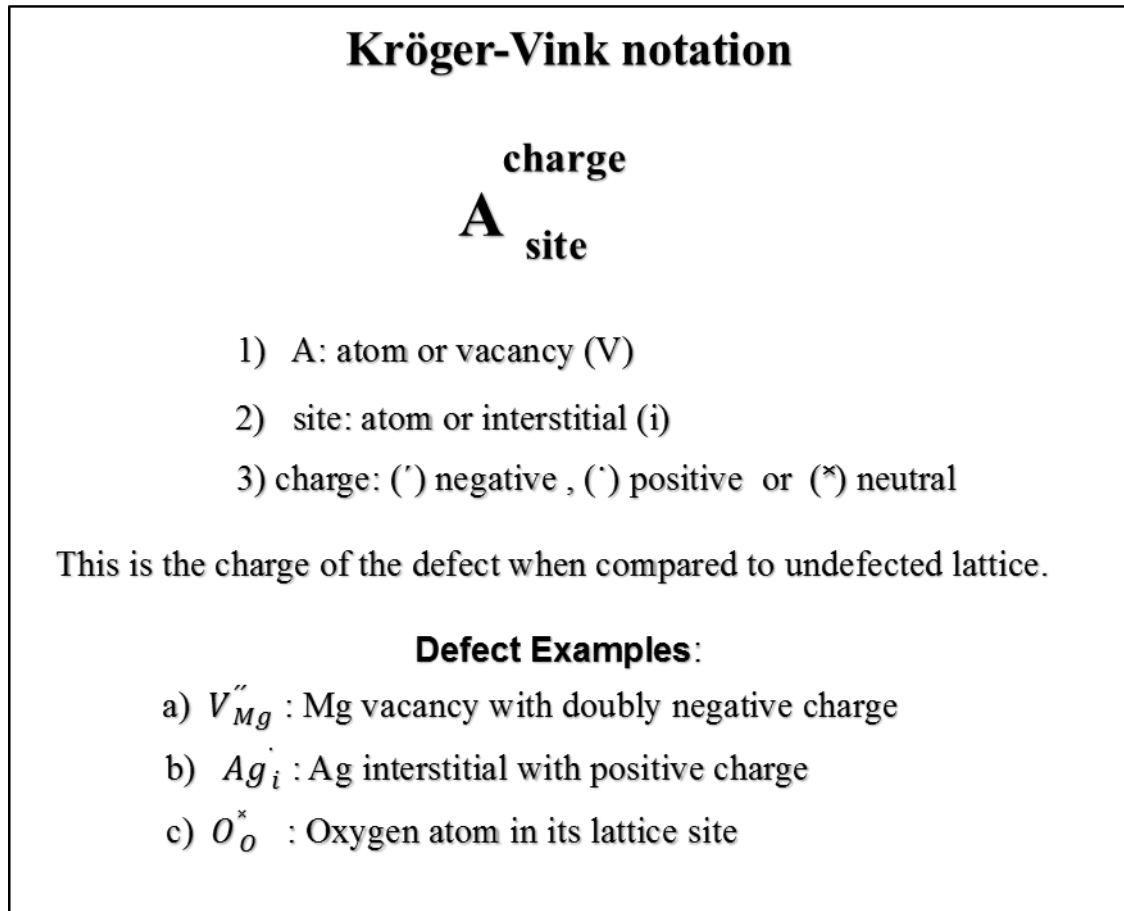
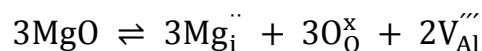


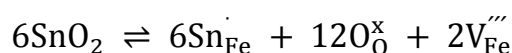
**Figure 8.** Point defect representation using the Kröger-Vink notation. Adapted from Van de Krol and Gratzel<sup>13</sup>.

b) Formation of a dilute solution of MgO in Al<sub>2</sub>O<sub>3</sub>:

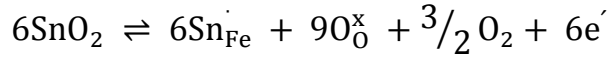


Charge and mass are balanced by the creation of three  $\text{Mg}_i''$  and two  $2\text{V}_{\text{Al}}'''$ . The anion to cation ratio is also maintained since three oxygen positions and two aluminum vacancies exist. The magnesium interstitials do not create more cation sites because interstitial sites exist before doping (Mg ions only use those interstitial sites).

Usually, metal oxides are doped with aliovalent ions, that is, ions that have a different charge to that of the metal ion. Aliovalent ions can react with metal oxides in two different ways: either by forming electronic defects or ionic defects, or by creating both electronic and ionic defects<sup>19; 20</sup>. For example, the incorporation of SnO<sub>2</sub> into Fe<sub>2</sub>O<sub>3</sub> can be done by creating ionic defects as follows:

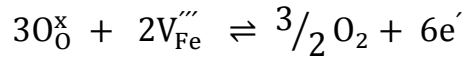


In this case, the creation of six Sn substitutional defects have been compensated by formation of two Fe vacancies. Another mechanism by which the formation of solid solution of SnO<sub>2</sub> in Fe<sub>2</sub>O<sub>3</sub> can be done is creating electronic defects:



This reaction shows that electrons are promoted to the conduction band when forming Sn substitutional defects.

The ionic compensation equation can be subtracted from the electronic compensation equation in order to know what conditions stimulate a particular mechanism:



According to this equilibrium reaction, the iron vacancies are favored at high oxygen pressure conditions, whereas electronic compensation is preferred at low concentration of the dopant and low oxygen pressure.

On the Kröger-Vink notation, it was assumed that all the ionic defects are completely ionized. However, the degree in which ionic defects become ionized depends on their energy of ionization. In addition, ionic defect levels close to the conduction or valence band edges are called shallow defects; on the contrary, ionic defect levels away from the band edges are denominated deep defects. Moreover, depending on their ionization charge, ionic defects can act either as donors or acceptors of electrons. In general, positively-charged ionic defects are donors because they have given up electrons, and, thus, becoming positively charged in relation with the host lattice; similarly, ionic defects with negative charge are acceptors since they have gained electrons<sup>20</sup>. The defects levels of Cu-doped ZnO are shown in Figure 9.

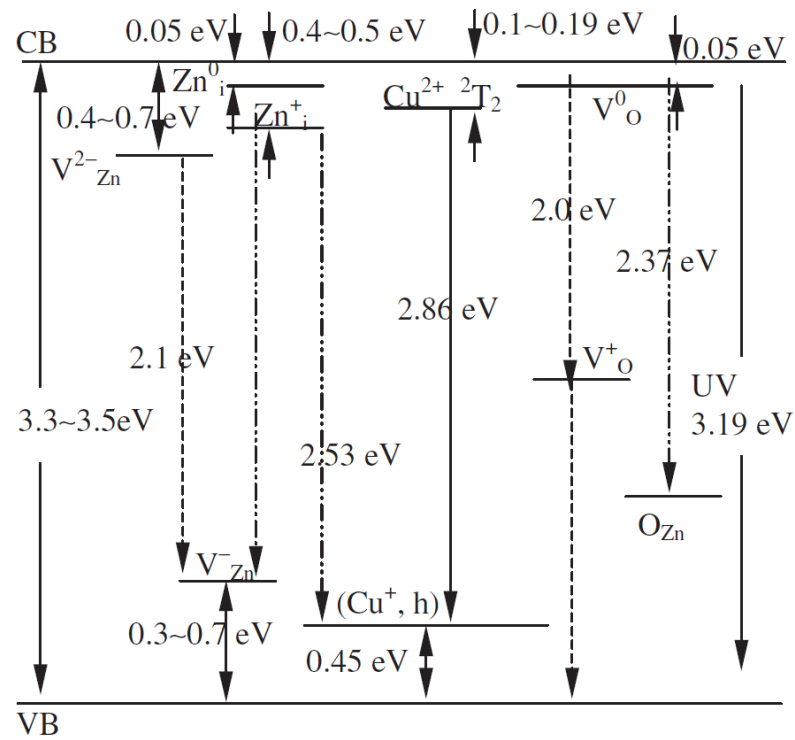


**Figure 9.** Point defect levels of Cu-doped ZnO causing different photoluminescence transitions<sup>21</sup>.

### 1.5 Iron oxide (hematite) as photoanode

Alpha iron oxide or hematite is one of the most widely studied semiconductors for applications in photoelectrochemical cells. Hematite, belonging to the space group  $R\bar{3}c$ , has a hexagonal structure containing six formula units per unit cell (Figure 10). In the hematite structure, oxygen atoms form hexagonal close-packed planes, while iron atoms occupy two thirds of the octahedral interstitial sites<sup>22</sup>. In addition, this ceramic is an abundant material, stable in neutral and basic solutions, inexpensive and appears as an N-type semiconductor due to presence of oxygen vacancies. Hematite has a 2.0-2.2 eV band gap which allows it to absorb approximately 40% of the incident solar spectrum on earth. In addition,  $\alpha\text{-Fe}_2\text{O}_3$  is used as photoanode because of its suitable conduction and valence band position for water oxidation. However, hematite possesses some limitations for its application in the photolysis of water. The average life time of the photoexcited electron-hole pair is short ( $\sim 10^{-12}$  s), which causes the hole diffusion length to be also short (2-4 nm). Moreover,  $\alpha\text{-Fe}_2\text{O}_3$  has a low conductivity and low charge-carrier mobility ( $< 1\text{cm}^2\text{ V}^{-1}\text{ s}^{-1}$ )<sup>23; 24</sup>.

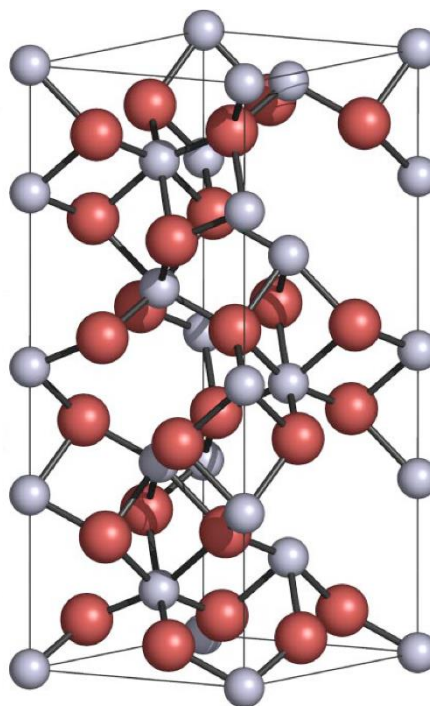


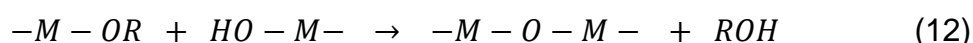
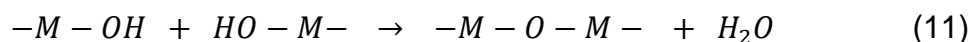
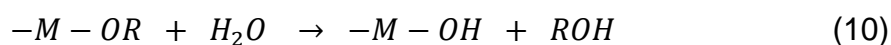
**Figure 10.** Hexagonal unit cell of  $\alpha\text{-Fe}_2\text{O}_3$ . Red and blue spheres represent oxygen and iron atoms, respectively<sup>25</sup>.

One approach to improve the performance  $\alpha\text{-Fe}_2\text{O}_3$  electrodes is doping them with metal ions. The main purpose of doping is to increase conductivity by increasing the charge carrier concentration. In particular, iron oxide has been doped with metal cations with 4+ charge such as  $\text{Ti}^{26}$ ,  $\text{Sn}^{27}$ ,  $\text{Si}^{28}$ , which demonstrate that doping increased hematite conductivity and positively influenced its photoresponse. Hematite was also doped with metal cations with a 2+ charge such as  $\text{Zn}^{29}$  which, though hematite's charge carrier concentration decreased, had a catalytic effect (decreased the photocurrent onset potential) and led to a better photocurrent. It is also possible that divalent metal cations can act as donors as demonstrated by Liu<sup>30</sup> et al. who doped hematite with  $\text{Ni}^{2+}$ , and results confirmed nickel cation improved iron oxide's photocatalytic response. In this work, the influence of two dopants with different charges ( $\text{Sn}^{4+}$  and  $\text{Zn}^{2+}$ ) on the hematite electrode performance is studied.

## 1.6 Polymerized Complex Method

Alpha iron oxide films have been prepared by various methods: hydrothermal<sup>31; 32</sup>, electrodeposition<sup>33</sup>, chemical vapor deposition<sup>34</sup>, atomic layer deposition<sup>35</sup> and spray pyrolysis<sup>36</sup>. A different method also used for deposition hematite films is the sol-gel method<sup>37; 38</sup>.

Sol-gel method is one of most used technologies for preparing metal oxides films. It offers two main advantages: a) homogeneous and stoichiometric compounds and b) low cost processing. The method starts with a molecular precursor which passes through two chemical stages: the formation of colloidal particles in a liquid phase (sol) which then turn into a three-dimensional network (gel). Metal oxide films can be obtained by the successive deposition of the sol-gel on a substrate and an adequate heat treatment<sup>39</sup>. Metal alkoxides are one type of the precursor used in the technique. Metal alkoxides undergo hydrolysis and condensation when in contact with water (sol). In the hydrolysis reaction (Eq. 10), OH groups bounded to the metal are formed, while in the condensation these hydrolyzed monomers can react to form metal-oxygen-metal bonds. These bonds are formed either by the reaction of two hydrolyzed monomer (dehydration, Eq. 11) or by the reaction of a hydrolyzed monomer and the metal alkoxides (dealcoholation, Eq. 12)<sup>39; 40; 41; 42</sup>. Inorganic polymers (gel) are, thus, formed by a progressive condensation.



There are two other kinds of methodologies that do not fit strictly into the previous sol-gel process but are also considered sol-gel techniques. These routes are the polymerized complex (PC) method and the polymer precursor (PP) method which involve the presence of organic polymers acting as the gel. Metal cations are stabilized by coordinating organic polymers that can be formed in situ or not. In the polymer precursor method a viscous solution is prepared by mixing an adequate polymer and metal oxide precursor in a suitable solvent. The polymerized complex method refers to the coordination of the metal ion by a chelating molecule that simultaneously undergoes polymerization<sup>41</sup>.

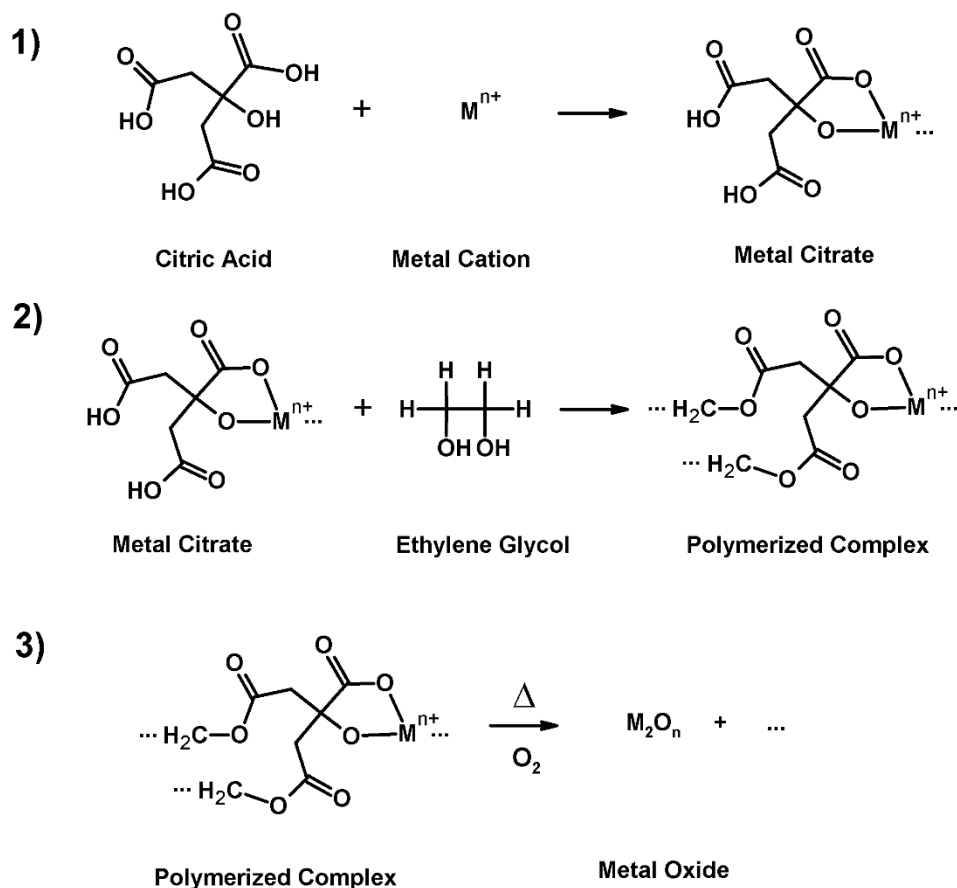


**Figure 11.** Pechini method sequence for the preparation of metal oxides.

The Pechini method is an example of the PC method (Figure 11). This method uses a polycarboxylic acid and a polyalcohol as precursors for the polyesterification reaction. Citric acid and ethylene glycol are commonly used as the polycarboxylic acid and polyalcohol, respectively, to form the polymer network. Citric acid has three carboxyl groups and has been used because it stabilizes non-monovalent metal cations very well.

Different types of complexes formed between the Fe (III) ion and citric acid are possible. The complex chemical structure is determined by various parameters such as the pH, solvent and molar ratio<sup>43; 44</sup>. However, the most important characteristic of this complex is that the oxygen from OH and COOH groups is involved in the complexation of Fe (III) ion<sup>45</sup>.

## 2. ADVANCES IN POLYMERIZED COMPLEX METHOD BY LEAN

In previous works done in our group, the influence of thermal treatment temperature on the preparation of hematite films was studied<sup>22</sup>. Hematite films were prepared by using a hydrothermal methodology in which akaganeite films are first obtained, and then akaganeite films are converted into hematite films by an additional thermal treatment. The akaganeite films were thermally treated at four different temperatures (390, 450, 550, and 800°C) for one hour. The results showed that pure hematite films are obtained at above 500°C, while films composed of a mixture of phases (akaganeite and hematite) are obtained at lower temperatures. Therefore, based on hydrothermal method results, in this work hematite films were prepared by the PC method at 500°C since only hematite phase is obtained.

In addition, thermal treatment at higher temperatures, such as 800°C, has demonstrated to improve the photocatalytic properties of hematite films in comparison with thermal treatments at lower temperatures<sup>46</sup>. In this context, our research group has also prepared hematite films by a hydrothermal method in which the additional thermal treatment temperature was high (750°C for 30 minutes), demonstrating that hematite films can generate higher photocurrents when prepared at higher temperatures<sup>47; 48</sup>. Thus, based on these previous results, hematite films prepared by the PC method were also prepared at higher temperatures (800°C for 30 minutes).

On the other hand, regarding the advances in the preparation of hematite films prepared by PC method, our group first studied the photoelectrochemical properties of pure hematite films and hematite films modified with silicon prepared at 500°C, in which the precursor solution was prepared in water<sup>49</sup>. Although the results showed that silicon improved the photocurrent density at 1.23 V<sub>RHE</sub>, some concentration of silicon segregated at the grain boundaries. Later, undoped and modified hematite films were prepared under the same conditions but the precursor solution was prepared in ethanol<sup>50</sup>. By using ethanol as solvent, doping of silicon into the hematite structure was successfully achieved. Nevertheless, it was observed that hematite films did not completely adhere to the FTO layer, that is, some areas of hematite films were not in contact with the FTO layer, which hindered the performance of hematite films. Therefore, this work aims to extend the previous investigations by studying the influence of annealing at a high temperature and



doping with metal ions on the performance of hematite films prepared by the PC method.

### **3. OBJECTIVES**

#### **3.1 General**

Prepare pure and modified iron oxide thin films as photoanodes in photoelectrochemical cells for hydrogen production.

#### **3.2 Specific**

- Synthesize pure and modified iron oxide electrodes by the polymerized complex method.
- Study the influence of doping and the thermal treatment on the photoelectrochemical properties of iron oxide electrodes.

### **4. EXPERIMENTAL PROCEDURE**

#### **4.1 Preparation of undoped and modified iron oxide films**

Undoped and modified hematite films were prepared by using the polymerized complex method as reported by Souza and coworkers<sup>49</sup>.

The first step of the procedure consisted in preparing a solution of citric acid in absolute ethanol (Absolute, 99.5%, Synth), and followed by the addition of  $\text{FeCl}_3 \cdot 6\text{H}_2\text{O}$  under constant stirring until total dissolution. The molar ratio of the citric acid to metallic cations used was 3:1. At this stage, ethylene glycol was added to the red solution at 60-65°C to promote the polyesterification. The mass relationship between ethylene glycol and citric acid used was 40:60 wt%. The system was maintained under these conditions until obtaining the desired viscosity of the solution. For the preparation of the doped hematite films, the doping precursors were mixed with the solution containing  $\text{FeCl}_3 \cdot 6\text{H}_2\text{O}$  prior to the ethylene glycol addition. Moreover, 0.5 mol% of the doping precursors ( $\text{Zn}(\text{NO}_3)_2$  and  $\text{SnCl}_4$ ) was used in relation with the iron cation.

Hematite thin films were produced on glasses coated with fluorine-doped tin oxide (FTO) by the spin coating technique. Some drops of the solution were placed over a cleaned FTO glass substrate, and then the substrate was spun at 500 rpm (5s) and 7000 rpm (30s). Next, the substrate coated with the precursor solution was

dried on a hot plate at 60°C for approximately 3 minutes. The deposition and drying procedure was repeated until obtaining a homogeneous film. Finally, all the films were treated thermally at two temperatures: at 500°C for 2 hours and at 800°C for 30 minutes, in which the heating rate and cooling were 3°C/min and 1°C/min, respectively.

## 4.2 Characterization

The XRD patterns of the films were obtained by using a diffractometer (D8 Discover, Bruker-ASX) configured with a CuK $\alpha$  X-radiation source. Because hematite films were so thin, it was opted to use grazing-incidence X-rays set at 0.5° relative to the film plane. An atomic force microscope (AFM/SPM 5500, Agilent) was used to study the films' roughness in non-contact mode. All these characterizations were carried out at *Central Experimental Multiusuário* (CEM) at *Universidade Federal do ABC*. The morphological features of the films were analyzed by using a scanning electron microscope (SEM, FEI Inspect F50). Static contact angles formed between a sessile water drop and films' surface were measured by using a commercial drop shape analysis system (Attension Optical Tensiometer, Theta Lite, KSV / CAM101) at room temperature. Contact angle variations were evaluated during the first 60 seconds, and the average of the left and right angles were recorded.

Micro-Raman Spectroscopy (inVia model, Renishaw) was performed by using a 514nm laser and an 1800 l/mm grating. Absorbance spectra in the ultraviolet-visible region (UV-Vis) were collected in a spectrophotometer Varian Cary 50, and bare FTO substrates were used as the blank. On the other hand, photoelectrochemical measurements were performed in a three-electrode electrochemical cell by using a potentiostat/galvanostat ( $\mu$ Autolab III coupled with A Frequency Response Analyzer). Saturated Ag/AgCl electrode and platinum electrode were used as the reference electrode and counter electrode, respectively. The measurements were carried out in a NaOH solution (1M, pH= 13.6 at 25°C), and the prepared films acted as the working electrodes. It was used an AM 1.5G simulated sunlight (100mW/cm<sup>2</sup>) for the measurement of photocurrents in which hematite films were illuminated through the glass side. Linear Sweep Voltammetry and Chronoamperometry were performed under these conditions. The films were also studied by Electrochemical Impedance in the dark by using a potential

perturbation of 10mV. These measurements were carried out in the Laboratory of Alternative Energy and Nanomaterials (LEAN) at *Universidade Federal do ABC*.

## 5. RESULTS

### 5.1 Structural study

Distortion of the crystal structure of hematite must be caused by the creation of substitutional defects when doping. Considering that the ionic radius of hexacoordinated  $\text{Fe}^{3+}$  (high spin),  $\text{Sn}^{4+}$  and  $\text{Zn}^{2+}$  are 0.645, 0.69 and 0.74 Å<sup>51</sup>, respectively, we expect to observe a distortion in the unit cell dimensions when  $\text{Zn}^{2+}$  e  $\text{Sn}^{4+}$  ions substitute  $\text{Fe}^{3+}$  ion.

The X-ray diffraction technique was carried out in order to identify the crystallographic phase of undoped and modified films as well as to study the incorporation of the impurities. The X-ray diffraction patterns of the hematite films are depicted in Figure 12, in which the diffraction peaks were indexed by using the JCPDS card N° 33-0664 (referred to the standard hematite powder). The XRD patterns of undoped films prepared at 500°C and 800°C (Figure 12a) matched the XRD patterns of the standard hematite power very well, which confirmed, therefore, that undoped films crystallized in the hematite phase ( $\alpha\text{-Fe}_2\text{O}_3$ ). In addition, the diffraction peaks of fluorine-doped tin oxide were identified according to the JCPDS card N° 41-1445 ( $\text{SnO}_2$  cassiterite phase). Additional diffraction peaks due to other phases were not found.

The XRD patterns of films modified with  $\text{Sn}^{4+}$  and  $\text{Zn}^{2+}$  (Figure 12 b and c) were indexed, and they also corresponded with those of a standard hematite powder. Formation of other phases in the modified films was also not found. In relation with the films modified with  $\text{Sn}^{4+}$  (Figure 12b), the XRD peaks of  $\text{SnO}_2$  was attributed to the conducting layer F- $\text{SnO}_2$  since all the hematite films were deposited onto the FTO substrates. Nevertheless, we are aware of the possible formation of  $\text{SnO}_2$  due to the segregation of the  $\text{Sn}^{4+}$  dopant, and this topic is discussed later.

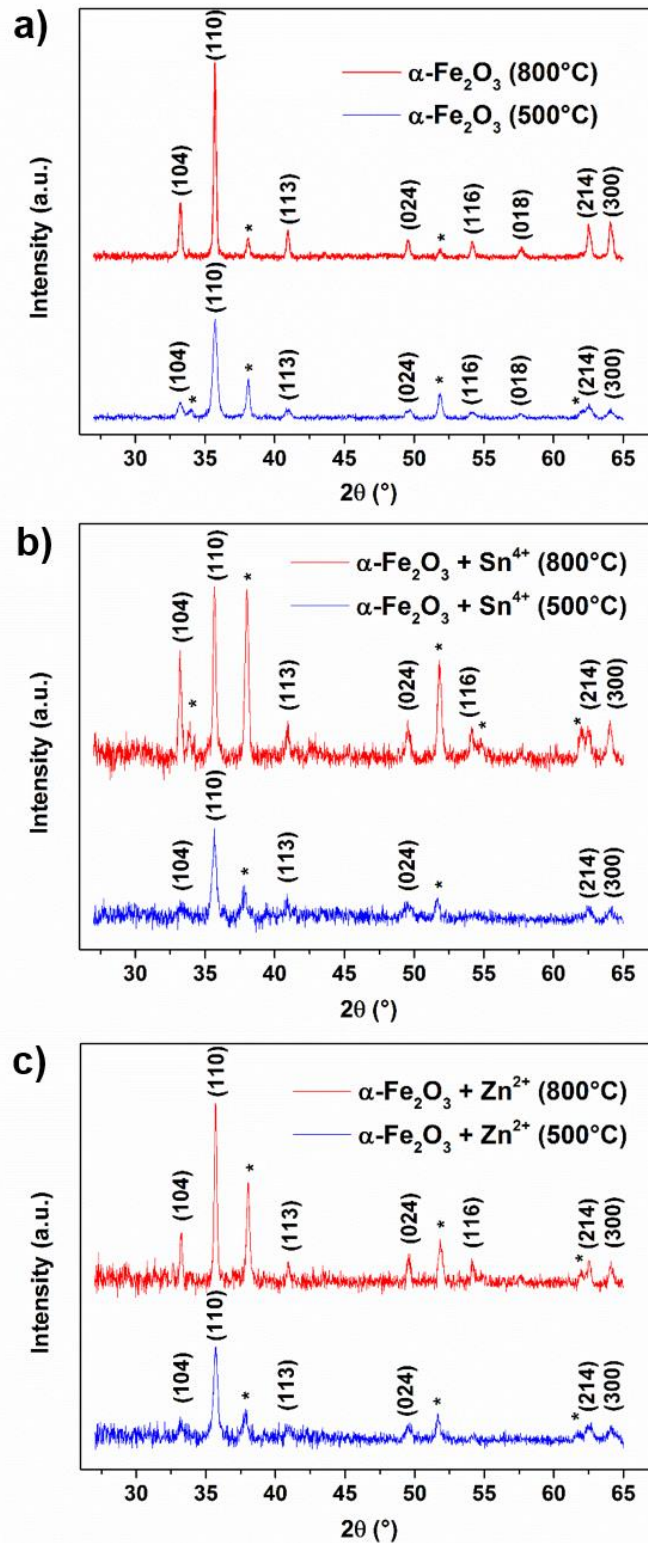


**Figure 12.** XRD patterns of hematite films prepared by the polymerized complex method with additional thermal treatment at different temperatures for (a) undoped hematite films, (b) Sn-modified hematite films and (c) Zn-modified hematite films. Diffraction peaks of the F-SnO<sub>2</sub> are indicated with asterisks.

Another way to study to the structural properties of the undoped and modified hematite films is by examining their unit cell parameters and cell volumes. By using the X-ray diffraction patterns and the free software named CellCal, those parameters were calculated and are displayed in Table 2. These parameters were close to those of the hematite crystallographic card which corroborated again that the films crystallized in the hematite phase. In addition, the lattice parameters and unit cell volume of the modified and undoped films were not significantly different.

**Table 2.** Lattice parameters, cell volume, orientation degree and hematite crystal size for undoped and modified hematite films obtained from XRD analysis. Hematite standard powder data was also included as reference.

Sample	a(Å)	c(Å)	V (Å <sup>3</sup> )	Highest <i>F</i> ( (110) plane)	Crystallite size (110) (nm)
JCPDS-33-0664	5.036	13,7	301.9		
$\alpha$ -Fe <sub>2</sub> O <sub>3</sub> (500°C)	5.024 (± 0.004)	13.767 (± 0.019)	300.985 (± 0.657)	0.45	22.1
$\alpha$ -Fe <sub>2</sub> O <sub>3</sub> + Sn <sup>4+</sup> (500°C)	5.022 (± 0.005)	13.797 (± 0.060)	301.377 (± 1.440)	0.35	23.8
$\alpha$ -Fe <sub>2</sub> O <sub>3</sub> + Zn <sup>2+</sup> (500°C)	5.022 (±0.005)	13.729 (± 0.056)	299.799 (± 1.334)	0.36	22.8
$\alpha$ -Fe <sub>2</sub> O <sub>3</sub> (800°C)	5.030 (± 0.001)	13.723 (± 0.005)	300.715 (± 0.171)	0.37	42.5
$\alpha$ -Fe <sub>2</sub> O <sub>3</sub> + Sn <sup>4+</sup> (800°C)	5.032 (± 0.001)	13.739 (± 0.010)	301.238 (± 0.279)	0.20	35.1
$\alpha$ -Fe <sub>2</sub> O <sub>3</sub> + Zn <sup>2+</sup> (800°C)	5.029 (± 0.001)	13.722 (± 0.007)	300.509 (± 0.197)	0.37	36.8

These last results may suggest that dopants were not incorporated into the hematite structure. However, another explanation for not observing a change in the cell parameters of modified films is related to the low dopant concentration used (0.5mol% of  $\text{Sn}^{4+}$  and  $\text{Zn}^{2+}$ ). That is, it is possible that the X-ray diffraction technique was not sensitive to the hematite structures modified with low concentration of dopants. For example, Uchiyama et al.<sup>52</sup> synthesized tin-doped hematite films by using higher concentration of tin (10 mol% and 25 mol%), in which the XRD peaks shifted slightly and it was attributed to doping. Therefore, a more sensitive technique is necessary to confirm whether or not hematite films were doped with metal ions.

The preferential orientation of the hematite crystallites was determined by using the XRD data (Figure 12) and equation 13. This parameter is an important requirement because studies reveal that hematite displays an anisotropic conductivity which changes according to the crystallographic planes exposed.

The degree of the preferential orientation can be calculated by using the Lotgering's equation<sup>53</sup>:

$$F = \frac{(P - P_0)}{(1 - P_0)} \quad (13)$$

where  $P = \sum I(h00) / \sum I(hkl)$ ,  $I$  is the diffraction peak intensity and  $P_0$  is the same as  $P$  for the non-oriented sample (in this case, pure hematite powder).

According to the results (Table 2), undoped and modified hematite films both prepared at 500°C and 800°C presented a preferential orientation to the (110) plane (the highest  $F$ ). Therefore, the iron oxide precursor solution prepared by the polymerized complex method and deposited on the FTO substrate allows to growth hematite films oriented preferentially at (110) plane.

It is well known that the hematite (001) basal plane may have a conductivity up to 4 orders of magnitudes higher than orthogonal planes to it<sup>54</sup>. Therefore, for applications as photoanodes in PECs, it is desirable to have most of the hematite crystal faces exposed at (001) plane, perpendicular to the substrate, in order to improve the charge separation (under illumination conditions) which favors the chemical reaction at the solid-liquid interface. The overall consequence of this preferential orientation is a gain in the photocatalytic performance of hematite films.

Additional, from the XRD diffraction data, the crystallite size of hematite films were determined by using the equation of Scherrer<sup>55</sup> :

$$L = \frac{K\lambda}{\beta \cos\theta} \quad (14)$$

where  $\lambda$  is the X-ray wavelength (nm),  $K$  is a constant which depends on the crystallite shape, crystallite-size distribution and how the width is determined, but it is usually taken as 0.9<sup>56</sup>;  $\theta$  is angle (radians) and  $\beta$  is the diffraction peak width at half maximum height. The estimated crystalline sizes were calculated from the diffraction peak of (110) plane and are summarized in Table 2. These results showed that the size of the hematite crystalline were lower for films prepared at 500°C in comparison with those of the hematite films treated at 800°C. In relation with effect of dopants, the modified hematite films prepared at 800°C had a lower crystalline size than that of the undoped film. However, for films synthesized at 500°C, both the undoped and modified hematite films exhibited approximately the same crystalline size.

## 5.2 Raman spectroscopy

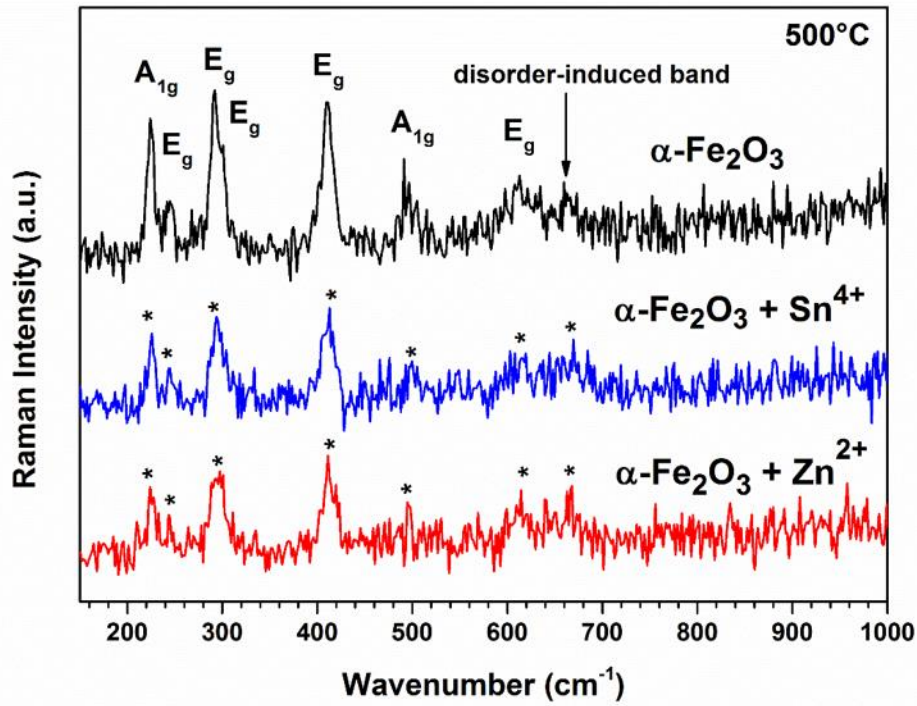
As mentioned above, the XRD technique was not able to identify the presence of the dopants added during the film preparation. In order to overcome that problem, Raman Spectroscopy was used because it is able to measure the local order and disorder by monitoring the vibrational modes of chemical bonds (Figure 13). As shown in Figure 13a, the seven characteristic vibrational modes of hematite were found and labeled for the undoped film<sup>57</sup>. In contrast, some vibrational modes were not found for modified films, as indicated with asterisks. In Figure 13b, both the undoped and modified films exhibited the seven modes of hematite, as predicted by the group theory analysis (summarized in Table 3).

Since hematite belongs to the point group  $D_{3d}$ , it possesses six different irreducible representations (Table 3). Among the irreducible vibration modes of hematite, only the  $A_{1g}$  and  $E_g$  modes are Raman active, and, theoretically, hematite should exhibit four  $E_g$  modes and two  $A_{1g}$  modes<sup>57</sup>.

The irreducible representation is designated by A when it is symmetric with respect to principal rotation operation, while the letter E means a twofold degenerated vibration. Moreover, the subscript  $g$  means that the irreducible representation is symmetric with respect to inversion, while the subscript  $1$  is used to designate a representation symmetric with respect to the  $C_2$  operation

perpendicular to the principal axis. Reader is referred to excellent books for a more extensive description of a character table<sup>58; 59</sup>.

a)



b)

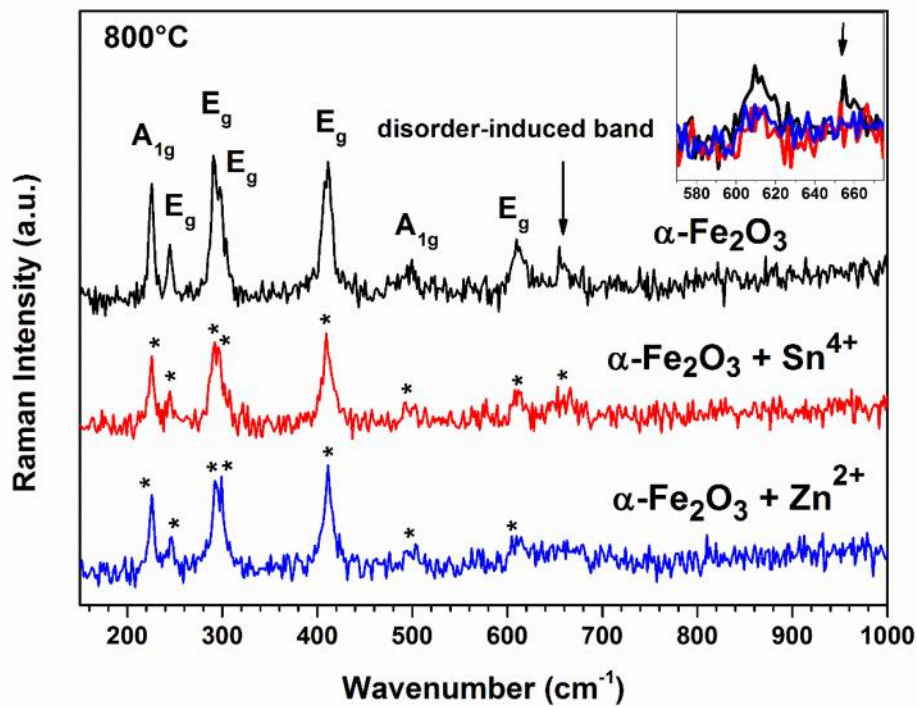


**Figure 13.** Raman spectra: a) films prepared at 500°C, b) films prepared at 800°C. Well-defined bands are indicated with asterisks.



**Table 3.** Character table of the point group  $D_{3d}$ .

$D_{3d}$	E	$2S_6(z)$	$S_6^2 \equiv 2C_3$	$S_6^3 \equiv S_2 \equiv i$	$3C_2$	$3\sigma_d$		
$A_{1g}$	+1	+1	+1	+1	+1	+1		$\alpha_{xx} + \alpha_{yy}, \alpha_{zz}$
$A_{1u}$	+1	-1	+1	-1	+1	-1		
$A_{2g}$	+1	+1	+1	+1	-1	-1	$R_z$	
$A_{2u}$	+1	-1	+1	-1	-1	+1	$T_z$	
$E_g$	+2	-1	-1	+2	0	0	$(R_x, R_y)$	$(\alpha_{xx} - \alpha_{yy}, \alpha_{xy}), (\alpha_{yz}, \alpha_{xy})$
$E_u$	+2	+1	-1	-2	0	0	$(T_x, T_y)$	

In addition to those bands, a band at about  $660\text{ cm}^{-1}$  was also labeled. According to the literature, this band can be originated from magnetite residues or the presence of crystal disorder in hematite lattice<sup>60; 61; 62</sup>. Since x-ray diffraction results did not show the presence of other phase, the  $660\text{ cm}^{-1}$  band originated due to the crystal disorder of hematite.

It was reported that the disorder-induced band intensity increases when a dopant is incorporated into the hematite lattice<sup>60; 63</sup>. This increase in the intensity was interpreted as dopants creating more defects. Moreover, another mechanism by which the intensity of this band can also increase is by decreasing the crystallite size of hematite. In contrast to what was found in literature, Raman spectra of  $800^\circ\text{C}$ -treated hematite films showed that the intensity of the band at about  $660\text{ cm}^{-1}$  decreased with the addition of  $\text{Sn}^{4+}$ ; and, the disorder-induced band practically disappeared for the Zn-modified hematite film (inset, Figure 13b). Therefore, this effect can be understood as the dopants improving the crystallinity of the hematite lattice. In other words, dopants are involved in the hematite lattice in a different way from that reported in literature. Another possible explanation of the decreasing of the  $660\text{ cm}^{-1}$ -band intensity is that the feature sizes of the modified films were bigger than those of the undoped hematite film. This hypothesis can be evaluated with the SEM results.

On the other hand, it was not possible to study the relative intensities of the  $660\text{ cm}^{-1}$  band of  $500^\circ\text{C}$ -treated films because of the high instrumental noise.

### 5.3 Morphological study

The morphological characteristics of the films were studied by scanning electron microscopy (Figure 14). According to the SEM images, all hematite films were observed to be composed of grains with a worm-like morphology as reported previously by Souza et al<sup>49</sup>. Moreover, in comparison with the grains of films prepared at 500°C (Figure 14 a, c, e), higher grains (more voluminous) were formed for films prepared at 800°C (Figure 14 b, d, f). In addition, it was estimated the length of grains for each hematite film. With respect to the films prepared at 500°C, the mean lengths of the grains for undoped hematite film, Sn-modified hematite film, and Zn-modified hematite film were 182, 193, 189 nm, respectively. Regarding films prepared at 800°C, the mean lengths of the grains for the undoped hematite film, Sn-modified hematite film, and Zn-modified hematite film were 300, 265, 255 nm, respectively. The results indicated that the length of hematite grains did not increase much with increasing thermal treatment temperatures. Nevertheless, the grains of films prepared at 800°C were thicker than those of the hematite films prepared at 500°C, which caused the hematite grains of the 800°C-treated films to be bigger.

Due to worm-like grains, the measurements of grain length were not in good agreement with the crystallite sizes estimated from equation 14 (see Table 2). However, the crystallite sizes estimated from Scherrer equation also suggested that grains of films prepared at 800°C were bigger than those of films prepared at 500°C. Thus, those estimations were in accordance with the grain sizes obtained from SEM images.

Moreover, SEM images suggested that films treated at 500°C exhibited a smooth and compact surface, whereas the surface of 800°C-treated films was rougher and more porous. The roughness of the films was evaluated by AFM technique and is discussed later. It is well known that the low porosity of photoelectrodes limits their photocatalytic properties because of the little contact area between the electrolyte and nanostructure surface. Therefore, it is expected that 800°C treated films exhibit a better photocatalytic response than that of 500°C treated films.

As mentioned in the above paragraph, the grains of the 800°C-treated hematite films modified with Sn<sup>4+</sup> and Zn<sup>2+</sup> were smaller than those of the undoped hematite film. Since the grain growth is based on the diffusion processes, the

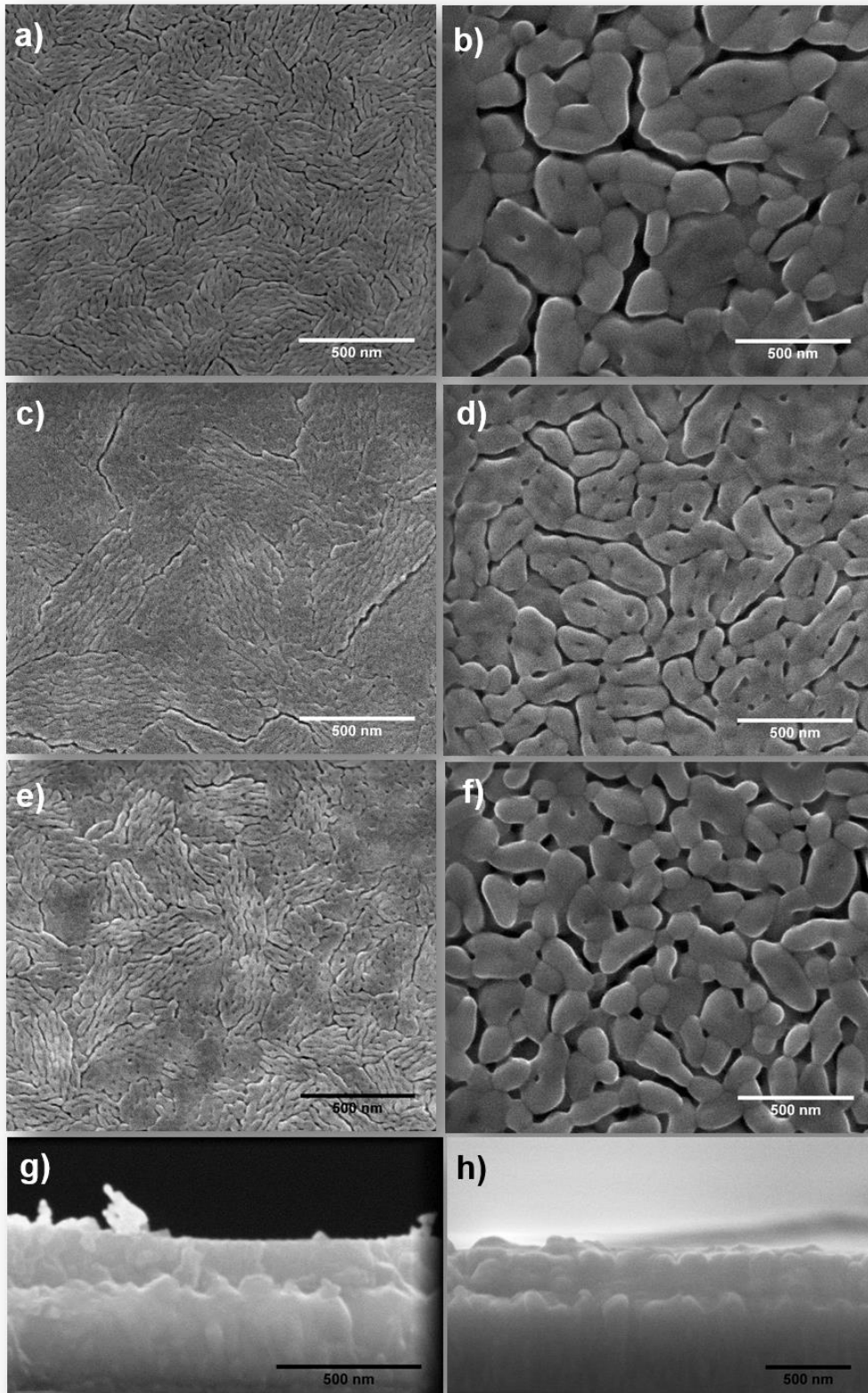


**Figure 14.** Top-view micrographs of hematite films: (a)  $\alpha$ -Fe<sub>2</sub>O<sub>3</sub> (500°C), (b)  $\alpha$ -Fe<sub>2</sub>O<sub>3</sub> (800°C), (c)  $\alpha$ -Fe<sub>2</sub>O<sub>3</sub> + Sn<sup>4+</sup> (500°C), (d)  $\alpha$ -Fe<sub>2</sub>O<sub>3</sub> + Sn<sup>4+</sup> (800°C), (e)  $\alpha$ -Fe<sub>2</sub>O<sub>3</sub> + Zn<sup>2+</sup> (500°C) f)  $\alpha$ -Fe<sub>2</sub>O<sub>3</sub> + Zn<sup>2+</sup> (800°C). Cross-section images of the undoped films prepared at (g) 500°C and (h) 800°C.

diffusion process for the growth of modified hematite grains was hindered. Thus, it is possible that to a certain degree the dopants  $\text{Sn}^{4+}$  and  $\text{Zn}^{2+}$  segregated at the grain boundaries, which made the hematite grains grow slowly. A similar result was found in the work of Souza et al.<sup>49</sup>, in which they prepared hematite films modified with silicon. The SEM images showed that the grains of the Si-modified hematite film were smaller than those of the undoped film. According to the XPS results, the authors concluded that silicon segregated in the grain boundaries of hematite. Therefore, segregation of the  $\text{Sn}^{4+}$  and  $\text{Zn}^{2+}$  into the modified hematite film may have occurred.

The SEM images were also useful to evaluate one of the hypothesis formulated in the Raman result discussion of 800°C-treated films. In that discussion, it was proposed that a possible explanation for the reduction in the intensity of the  $660\text{ cm}^{-1}$  band was because modified films had bigger grains. Nevertheless, in relation with the films prepared at 800°C, SEM images showed that the grains of the modified films were smaller than those of the undoped film (also suggested by equation 14, Table 2). Consequently, the decrease of the  $660\text{ cm}^{-1}$  band of doped films cannot be explained by considering the grain sizes. Therefore, the dopants could have improved the crystallinity of hematite lattice.

On the other hand, semiconductor films should have an adequate thickness in order to absorb most of sunlight irradiated. For example, a hematite film of 400 nm thickness can absorb approximately 95% of the sunlight intensity of a 550 nm wavelength<sup>64</sup>. In this context, the thicknesses of the undoped films prepared at 500°C and 800°C were measured (Figure 14g and 14h). The mean thickness of the 500°C-treated film was 162 nm, while the mean thickness of the 800°C-treated film was 285 nm. The greater thickness of the film prepared at 800°C can be related to their higher nanostructures that made the film more voluminous and porous. In contrast, the 500°C-treated film was thinner, and it can be attributed to small, well packed nanostructures.

## 5.4 Optical study

The optical properties of the undoped and modified hematite films were assessed by UV-Vis absorption spectroscopy (Figure 15). This technique was performed in order to explore the possible electronic changes in light absorption caused by the different temperatures of thermal treatment and the dopant insertion.

Furthermore, the incorporation of  $\text{Sn}^{4+}$  and  $\text{Zn}^{2+}$  as dopants can create sublevels between the conduction and valence band of hematite, which can affect the charge transfer process.

Fig. 15 illustrates the absorption coefficient versus wavelength spectra for all hematite films, in which the absorption spectra of the hematite films were normalized by the thicknesses estimated by the SEM measurements (Figure 14), and a bare substrate was used as the blank. Figure 15a shows that 500°C-treated hematite films had similar curve profiles, and the Sn-modified hematite film exhibited the highest absorption above 600 nm. On the contrary, spectra of films prepared at 800°C were significantly different (Figure 15b) in which modified films had a well defined band (above 600 nm) in comparison with the undoped film. These bands were centered at approximately 660 nm and 640 nm for the Sn-modified and Zn-modified hematite film, respectively.

Since pure hematite has a band gap of 2.2 eV (corresponding to a 550 nm wavelength), these low energy bands may be related to intermediate energy levels between the conduction and valence band. Intermediate energy levels can be formed due to the presence of point defects such oxygen vacancies or the incorporation of dopants<sup>65; 66; 67</sup>.

The optical band gap energy of hematite films were calculated by using the following equation:

$$\alpha h\nu = \beta(h\nu - E_g)^m \quad (15)$$

where  $\beta$  is a constant,  $E_g$  is the optical band gap and  $m$  is a number whose value depends on the type of electronic transition. The variable  $m$  is equal to  $\frac{1}{2}$  for a direct electronic transition (corresponded to  $\text{Fe}^{3+}$  d orbitals), whereas it is equal to 2 for an indirect electronic transition (from the  $\text{Fe}^{3+}$  d orbital to the  $\text{O}^{2-}$  2p orbital)<sup>68</sup>. The optical band gap can be extracted from the x-axis intersection of the linear fitting of the curve  $(\alpha h\nu)^{1/m}$  versus  $h\nu$ , which are depicted in Figure 16a,b and 16 c,d for  $m=\frac{1}{2}$  and  $m=2$ , respectively. The estimated values of the direct and indirect optical band gap are summarized in Table 4.

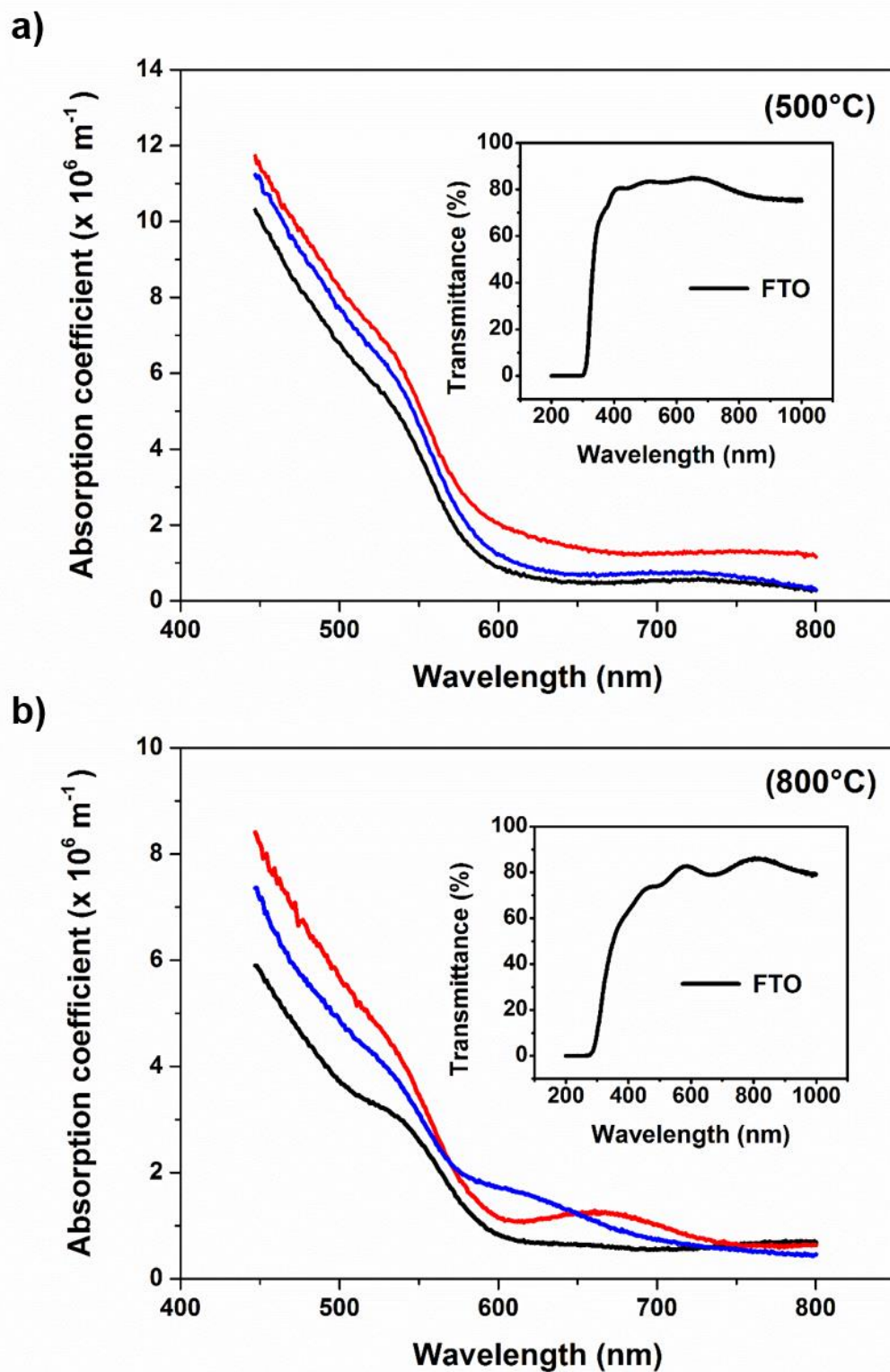


**Figure 15.** Absorption coefficient as function of wavelength of hematite films treated at (a) 500°C and (b) 800°C: -----  $\alpha\text{-Fe}_2\text{O}_3$ , - - - -  $\alpha\text{-Fe}_2\text{O}_3 + \text{Sn}^{4+}$ , - - - -  $\alpha\text{-Fe}_2\text{O}_3 + \text{Zn}^{2+}$ . Inset graphs show the transmittance spectrum of the FTO substrate.

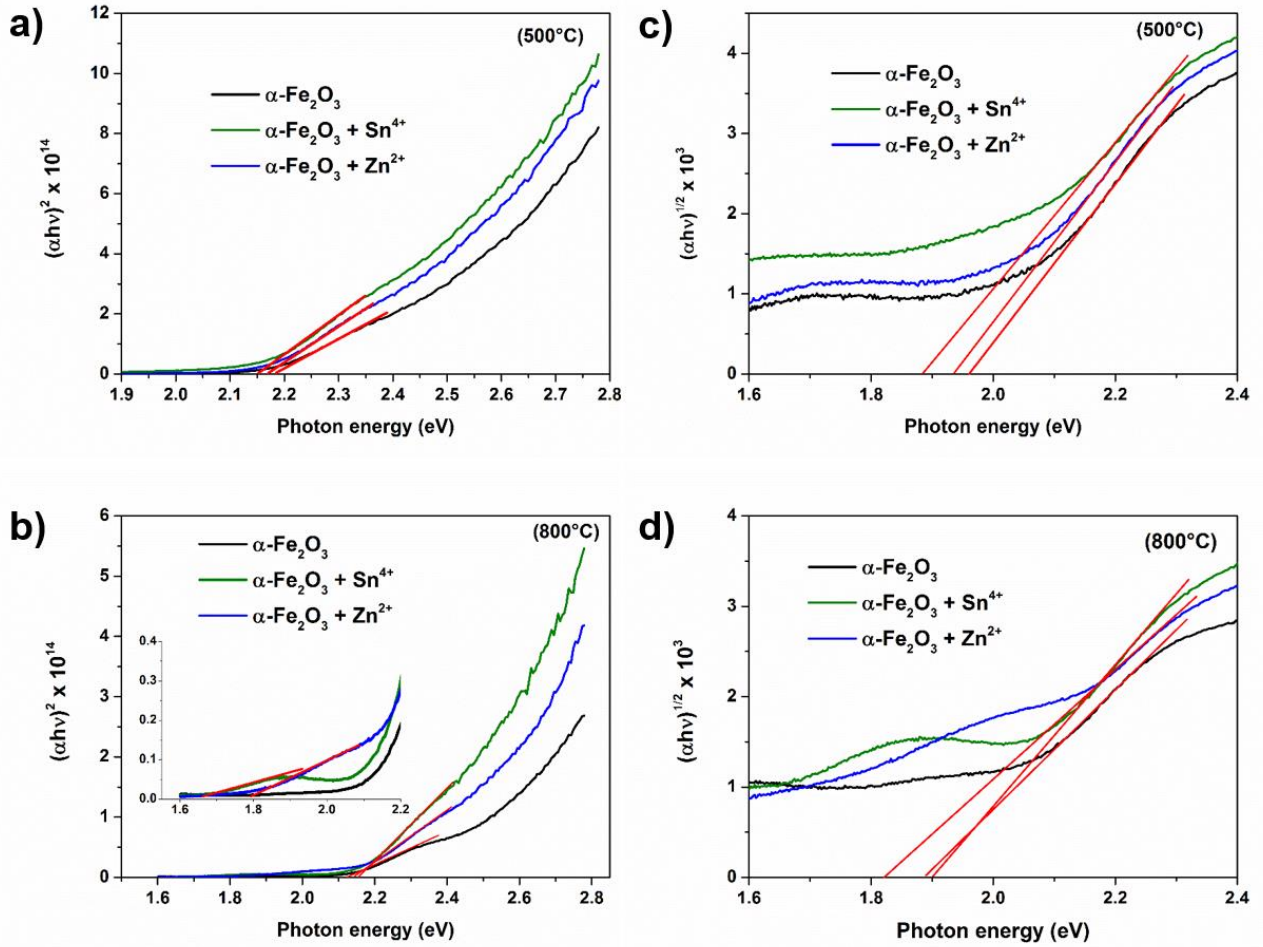


**Figure 16.** Calculation of the direct electronic transition of electrodes prepared at (a) 500°C and (b) 800°C. Calculation of the indirect electronic transition of hematite electrodes prepared at (c) 500°C and (d) 800°C.

**Table 4.** Estimated direct and indirect electronic transitions of all the synthesized hematite films.

Sample	Direct $E_g$ (eV)	Indirect $E_g$ (eV)
$\alpha\text{-Fe}_2\text{O}_3$ (500°C)	2.18	1.96
$\alpha\text{-Fe}_2\text{O}_3 + \text{Sn}^{4+}$ (500°C)	2.15	1.88
$\alpha\text{-Fe}_2\text{O}_3 + \text{Zn}^{2+}$ (500°C)	2.17	1.93
$\alpha\text{-Fe}_2\text{O}_3$ (800°C)	2.13	1.89
$\alpha\text{-Fe}_2\text{O}_3 + \text{Sn}^{4+}$ (800°C)	2.15; 1.65	1.90
$\alpha\text{-Fe}_2\text{O}_3 + \text{Zn}^{2+}$ (800°C)	2.14; 1.79	1.82

The estimated direct and indirect optical band gap values were close to those reported in literature<sup>69; 70</sup>. In addition, intermediate electronic transitions were identified for the modified hematite films prepared at 800°C as previously suggested by the absorbance coefficient graphs (Figure 15b). These intermediate electronic levels can improve the photocatalytic properties of hematite or act as recombination sites. The photoelectrochemical results of these electrodes can give insight into the function of these intermediate levels (it will be discussed in the next section).

So far, the fundamental properties of the hematite films were studied, and the effect of the dopants and thermal treatment temperatures on hematite films' properties were also discussed. In the following section, the performance of the hematite films as photoanodes for the water oxidation will be evaluated.

### 5.5 Photoelectrochemical study

The electrochemical performances of the synthesized films were evaluated in a half cell configuration, both in the dark and under illumination, by means of linear sweep voltammetry (Figure 17). The experiments were carried out in a 1M NaOH solution (pH=13.6 at 25°C) at scan rate of 50mV/s, and the films were illuminated through the glass side. In addition, the Ag/AgCl reference potential used was converted into the reversible hydrogen electrode (RHE) by using the following equation:

$$V_{RHE} = V_{Ag/AgCl} + V_{Ag/AgCl \text{ vs. SHE}} + 0.059 \times pH \quad (16)$$

where  $V_{Ag/AgCl \text{ vs. SHE}}$  is the potential of the Ag/AgCl reference potential (in saturated KCl) with respect to standard hydrogen potential (SHE).

According to the linear sweep voltammograms (Figure 17), the oxygen evolution reaction (OER) took place at the surface of hematite films under dark conditions. Additionally, all the hematite films exhibited a catalytic response when they were illuminated, which confirmed that hematite films were able to absorb sunlight (visible range) and convert it directly into current (taking place also the OER). Regarding the OER in the dark, results showed that electrodes prepared at 500°C and 800°C exhibited different onset potentials for the OER. Oxygen evolution started at approximately 1.5  $V_{RHE}$  in 500°C-synthesized films (Figure 17 a,c,e) while oxygen evolution started at higher potentials for 800°C-synthesized films (Figure 17 b,d,f). When we regard the effect of dopants, Figure 17 f) shows that the Zn-modified



film displayed a lower potential for electrocatalytic oxygen evolution in comparison with the undoped and Sn-modified film (Figure 17 b and d). With respect to the OER under illumination conditions, the onset potentials of the photocurrent density were about 0.6 V<sub>RHE</sub> for all the hematite films except for Sn-modified hematite films prepared at 500°C (~0.65 V<sub>RHE</sub>, Figure 17 c) and at 800°C (~0.64 V<sub>RHE</sub>, Figure 17 d).

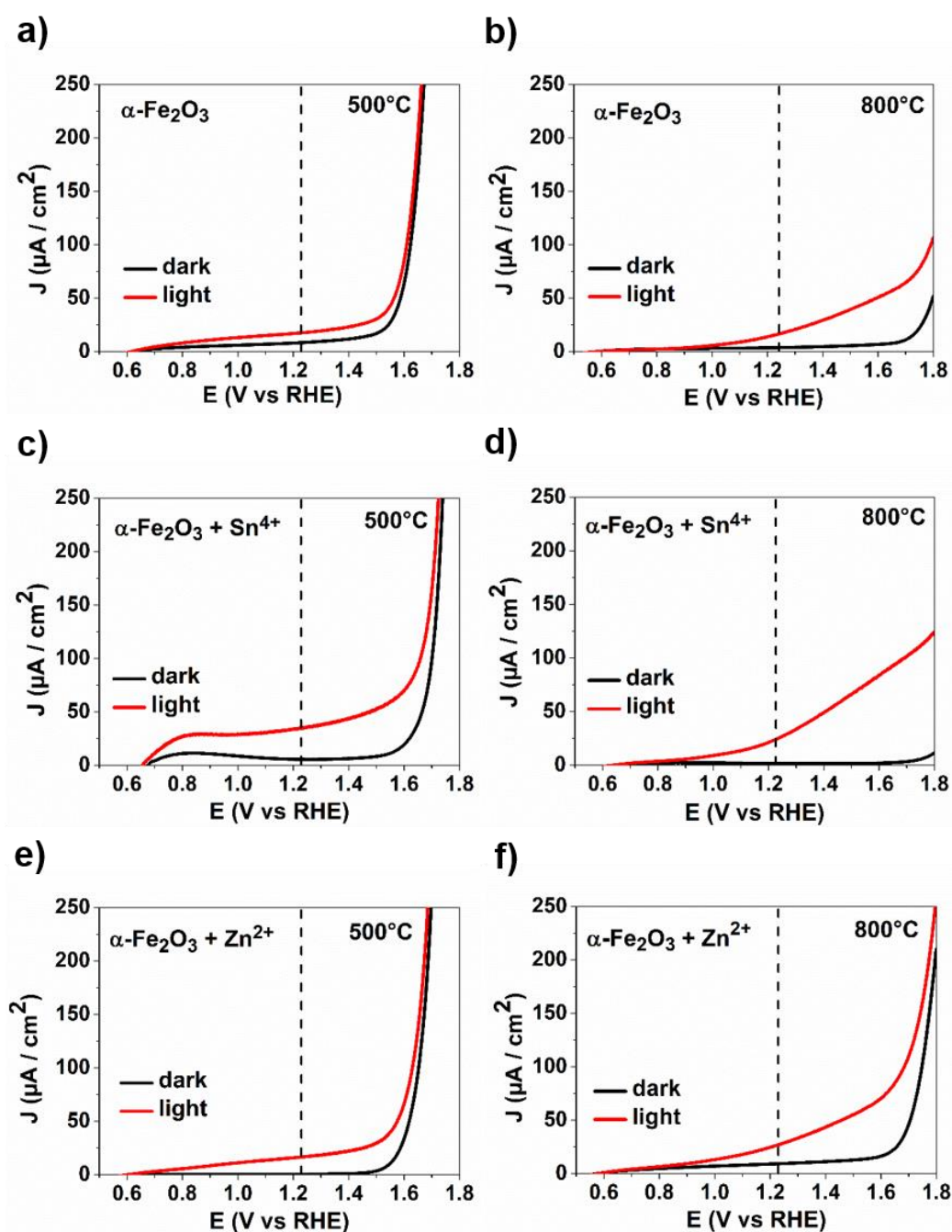


**Figure 17.** Linear sweep voltammograms: (a)  $\alpha\text{-Fe}_2\text{O}_3$  (500°C), (b)  $\alpha\text{-Fe}_2\text{O}_3$  (800°C), (c)  $\alpha\text{-Fe}_2\text{O}_3 + \text{Sn}^{4+}$  (500°C), (d)  $\alpha\text{-Fe}_2\text{O}_3 + \text{Sn}^{4+}$  (800°C), (e)  $\alpha\text{-Fe}_2\text{O}_3 + \text{Zn}^{2+}$  (500°C), and (f)  $\alpha\text{-Fe}_2\text{O}_3 + \text{Zn}^{2+}$  (800°C).

The photocurrent onset potential of hematite films is not the only parameter that should be considered when characterizing the photocatalytic properties of photoanodes. Most importantly, the photocatalytic performances of photoanodes films are assessed by examining their photocurrents generated at 1.23 V<sub>RHE</sub> (the thermodynamic potential for water oxidation). In this sense, the photocurrent densities of all the hematite films at 1.23 V<sub>RHE</sub> are summarized in Table 5.

**Table 5.** Photocurrent density,  $J$ , at 1.23 V<sub>RHE</sub> of hematite electrodes.

Hematite films	$J$ ( $\mu\text{A}/\text{cm}^2$ ) (1.23 V vs RHE)
$\alpha\text{-Fe}_2\text{O}_3$ (500°C)	17.7
$\alpha\text{-Fe}_2\text{O}_3 + \text{Sn}^{4+}$ (500°C)	34.8
$\alpha\text{-Fe}_2\text{O}_3 + \text{Zn}^{2+}$ (500°C)	17.0
$\alpha\text{-Fe}_2\text{O}_3$ (800°C)	15.8
$\alpha\text{-Fe}_2\text{O}_3 + \text{Sn}^{4+}$ (800°C)	24.6
$\alpha\text{-Fe}_2\text{O}_3 + \text{Zn}^{2+}$ (800°C)	27.2

The results of Table 5 were evaluated in two ways: by studying the effect of impurities on pure hematite films treated at the same temperature; and by studying the effect of heat temperature on films with the same composition. In the first case, films prepared at 800°C and modified with Sn<sup>4+</sup> and Zn<sup>2+</sup> exhibited a higher photocurrent than that of the undoped hematite film. For films prepared at 500°C, the incorporation of Sn<sup>4+</sup> on hematite improved the photocatalytic properties but the Zn-modified hematite film exhibited a reduction in the photocurrent. In the second case, the results suggested that, with exception of Zn-Fe<sub>2</sub>O<sub>3</sub>, the heat treatment at higher temperatures worsened the photocatalytic properties. These results were not expected since we expected all the dopants to enhance the hematite film performances<sup>52; 71</sup>. Furthermore, we also expected the 800°C-treated hematite films to have a better performance than those at prepared at 500°C because generally better performances of hematite films were achieved at higher temperature of thermal treatments<sup>72; 73</sup>.

In order to clarify the linear sweep voltammetry results and study the stability of the films, hematite electrodes were studied by chronoamperometry.

Chronoamperograms were recorded under illumination for one hour at constant voltage of 1.23 V<sub>RHE</sub> (Figure 18).

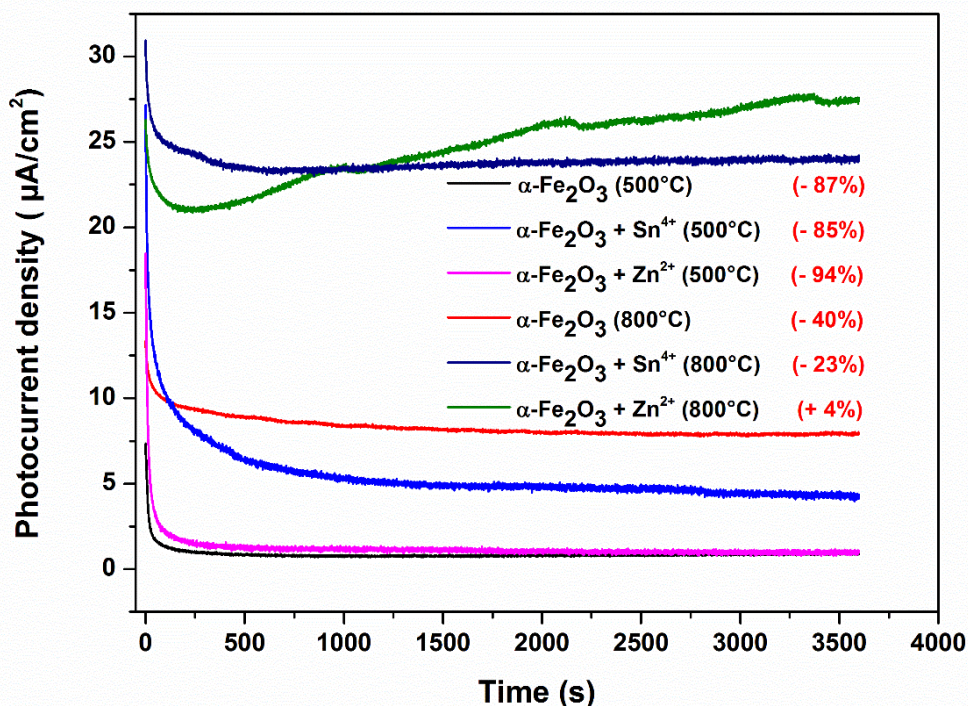


**Figure 18.** Photochronoamperograms of undoped and modified hematite films at 1.23 V<sub>RHE</sub>. The percent variation of the photocurrent is shown in red brackets

As shown in Figure 18, all the hematite films exhibited an initial photocurrent density which decreased during the first minutes and then stabilized and remained practically constant. That is, all the hematite films were not stable during the first minutes of the measurements. Therefore, the stability of the hematite films was assessed by calculating the percent variation of the initial and final photocurrent density (showed in Figure 18). As in the linear sweep voltammetry results, the chronoamperometry results were evaluated by studying the effect of thermal treatment and doping. As expected, the results showed that thermal treatment at higher temperatures improved the stability and the generated photocurrent, and they were quite different from the linear sweep voltammetry results (compare with Table 5). In addition, all the modified hematite films exhibited a better photocurrent when comparing with undoped hematite films except for the Zn-modified hematite film prepared at 500°C. These results were in good agreement with the results from

linear sweep voltammetry and confirmed that  $\text{Zn}^{2+}$  did not improve the catalytic response of the 500°C-treated hematite film under illumination conditions.

## 5.6 Electrochemical impedance (EIS)

The hematite electrodes were also studied by electrochemical impedance technique in darkness. This technique allows to obtain important electronic parameters such as the density of charge carriers ( $N_D$ ) and the flat band potential ( $V_{FB}$ ) of semiconductor films. For an n-type semiconductor being in the depletion layer condition, these parameters can be extracted from the following Mott-Schottky equation<sup>74</sup>:

$$\frac{1}{C^2} = \left( \frac{2}{q\epsilon\epsilon_0 N_D} \right) \left( V - V_{FB} - \frac{kT}{q} \right) \quad (17)$$

where  $C$  is the capacitance of the space charge region,  $q$  is the electron charge,  $\epsilon_0$  is the electric permittivity of free space,  $\epsilon$  is the semiconductor dielectric constant ( $\epsilon_{\text{Hematite}}=80$ )<sup>75</sup>,  $N_D$  is charge carrier density,  $V$  is the applied potential,  $V_{FB}$  is the flat band potential,  $k$  is the Boltzmann constant and  $T$  is the temperature. According to the Mott-Schottky equation, the plot of  $1/C^2$  versus  $V$  is a straight line whose slope and y-axis intersection provide the  $N_D$  and  $V_{FB}$  values, respectively.

The Mott-Schottky curves of the hematite films at 1kHz are shown in Figure 19. As noted, there is no single well-defined linear region in the Mott-Schottky plots. Most of the curves appeared to be concave downward, except for the curve of the Sn-modified hematite film (500°C) which seemed to have two linear regions.

A possible explanation for this phenomenon is that the synthesized films do not meet the conditions on which the Mott-Schottky equation is based. Some conditions that equation 17 is based on are the following: a) the electrolyte and the semiconductor have zero resistance; b) the system is free of surface states; c) the semiconductor dielectric constant is the same for all frequencies; d) the semiconductor-electrolyte interface is perfectly planar and two-dimensionally infinite and e) the influence of Helmholtz layer is not considered<sup>76</sup>.

The non-linearity of Mott-Schottky graphs can also be interpreted in a different way. This explanation is based on the research work of Leduc et al <sup>77</sup> and Horowitz<sup>78</sup> who studied two abnormal Mott-Schottky graphs of hematite electrodes: one being curved and the other having two linear regions. According to the authors,

the first abnormal curve can be originated from the existence of a deep donor level in the semiconductor. Moreover, they pointed out that the break in the  $1/C^2$  vs  $V$  curves (which creates two linear regions) is a characteristic of a semiconductor having both a deep donor level and a localized surface state.

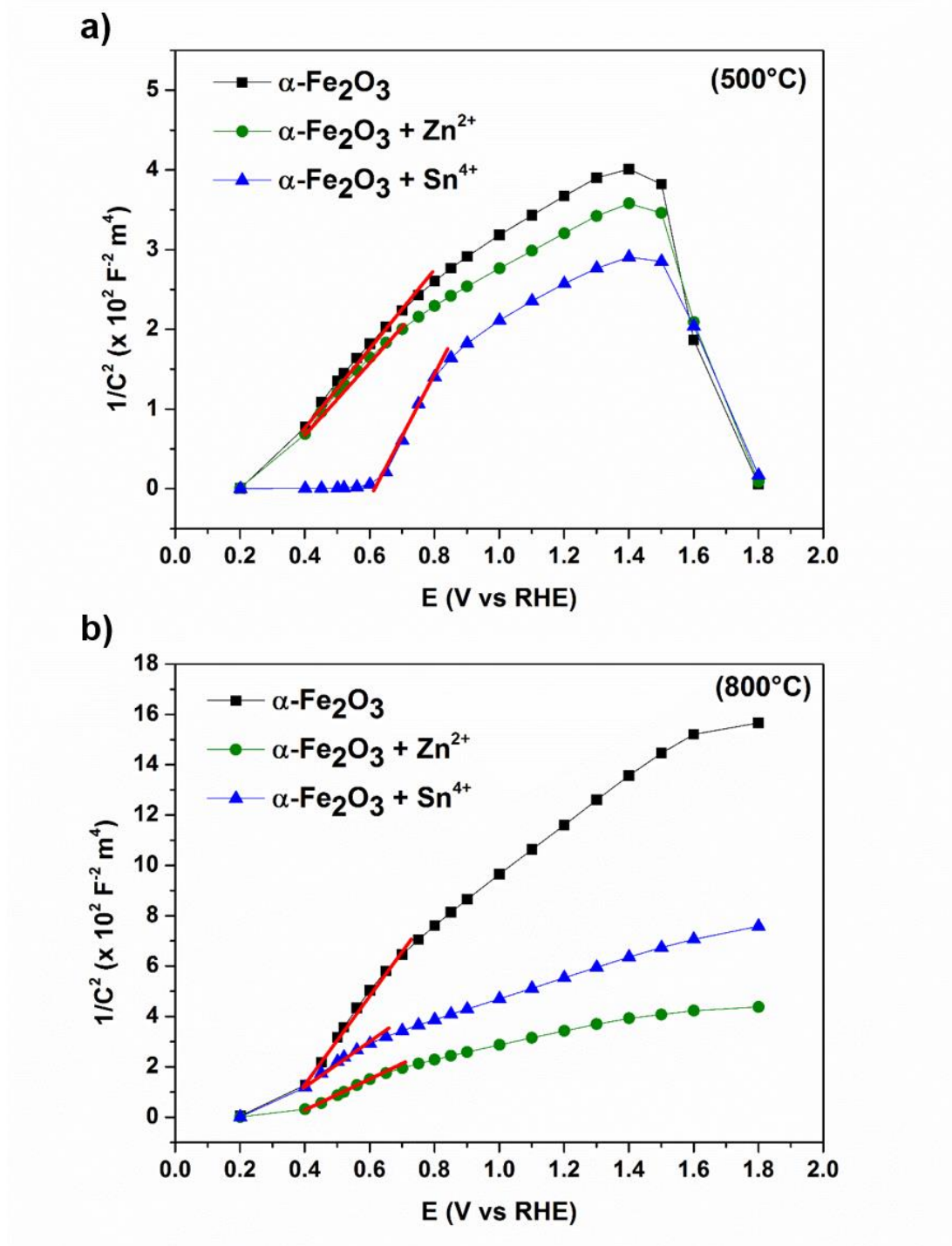


**Figure 19.** Mott-Schottky plots of hematite films prepared (a) at 500°C and (b) at 800°C.

Although the Mott-Schottky plots did not have a well-defined linear region, the  $N_D$  and  $V_{FB}$  values were estimated from the linear region started at low potentials (Figure 19) and they are shown in Table 6. The order of magnitude of  $N_D$  values is similar to that reported in literature<sup>73; 79; 80; 81</sup>. For films prepared at 500°C, results suggested that  $Sn^{4+}$  is acting as an acceptor while  $Zn^{2+}$  is acting as a donor. In contrast, the incorporation of both  $Sn^{4+}$  and  $Zn^{2+}$  dopants increased the  $N_D$  in hematite films synthesized at 800°C.

On the other hand, a typical value for  $V_{FB}$  is about  $0.5 V_{RHE}$ <sup>75; 82</sup> in which the experimental onset potential is around  $0.8 V_{RHE}$ . However, our results differ from those founded in literature in that the calculated  $V_{FB}$  values are lower (  $\sim 0.3 V_{RHE}$  for 800°C-treated films and  $\sim 0.20 V_{RHE}$  for 500°C-treated films) as well as the experimental onset potentials ( $\sim 0.6 V_{RHE}$ ). By using the theoretical flat band potentials and the photocurrent onset potentials, the pseudo-overpotentials of water oxidation ( $\eta_{ox}$ ) were calculated and are shown in Table 6. According to the results, most of the films exhibited large overpotentials but the Sn-modified hematite film synthesized at 500°C exhibited the lowest overpotential.

**Table 6.** Electronic parameters estimated from Mott-Schottky curves.

Film	$N_D$ ( $\times 10^{19} \text{ cm}^{-3}$ )	$V_{FB}$ (V vs $V_{RHE}$ )	$\eta_{ox}$	$W(\text{nm})$ at $1.23 V_{RHE}$
$\alpha\text{-Fe}_2\text{O}_3$ (500°C)	3.79	0.19	0.43	15.4
$\alpha\text{-Fe}_2\text{O}_3 + Sn^{4+}$ (500°C)	2.19	0.60	0.05	15.6
$\alpha\text{-Fe}_2\text{O}_3 + Zn^{2+}$ (500°C)	4.05	0.20	0.40	14.8
$\alpha\text{-Fe}_2\text{O}_3$ (800°C)	1.00	0.30	0.28	28.3
$\alpha\text{-Fe}_2\text{O}_3 + Sn^{4+}$ (800°C)	2.04	0.23	0.41	20.6
$\alpha\text{-Fe}_2\text{O}_3 + Zn^{2+}$ (800°C)	2.98	0.33	0.25	16.1

Moreover, the depletion layer width films ( $W$ ) of the undoped and modified hematite films were calculated by using the following equation:

$$W = \sqrt{\frac{2\epsilon\epsilon_0}{eN_D} \left( V - V_{FB} - \frac{kT}{q} \right)} \quad (18)$$

where all the variables and constants have the same meaning as those of constants in equation 18. The depletion layer width at 1.23  $V_{RHE}$  of the hematite films are shown in Table 6. The films prepared at 800°C exhibited depletion layer widths slightly larger than those of the films prepared at 500°C. Since the electric field intensity is higher for small depletion layer width, so, the smaller the depletion layer width, the better the separation of the photogenerated electron-hole pairs. Therefore, the charge separation of photogenerated hole-electron pairs into the 500°C-treated hematite films should be more efficient than that occurring into the 800°C-treated hematite films. However, since the performances of hematite films prepared at 500°C were not good as those of the films prepared at 800°C, it seems that the depletion layer width did not play an important role for the photogenerated charge separation.

### 5.7 Surface study

The hydrophilic properties of hematite films when interacting with the electrolyte can be investigated by measuring the contact angle formed between an electrolyte drop and the hematite film surface. Basically, the contact angle is defined as the angle formed between the surface film and the tangent line of the liquid surface. In this work, the contact angle of a water drop on the film surface was measured for all the hematite films. Figure 20 shows the drop shapes in contact with the surface of hematite films. Lower contact angles were observed for films prepared at 800°C than those of hematite films synthesized at 500°C. Interestingly, the addition of  $Sn^{4+}$  and  $Zn^{2+}$  on hematite films reduced the contact angles when compared with those of the undoped sample for films prepared at the same temperature. In addition, Table 7 shows the average contact angles (arithmetic mean of the left and right angles) which are in good agreement with the previous description.

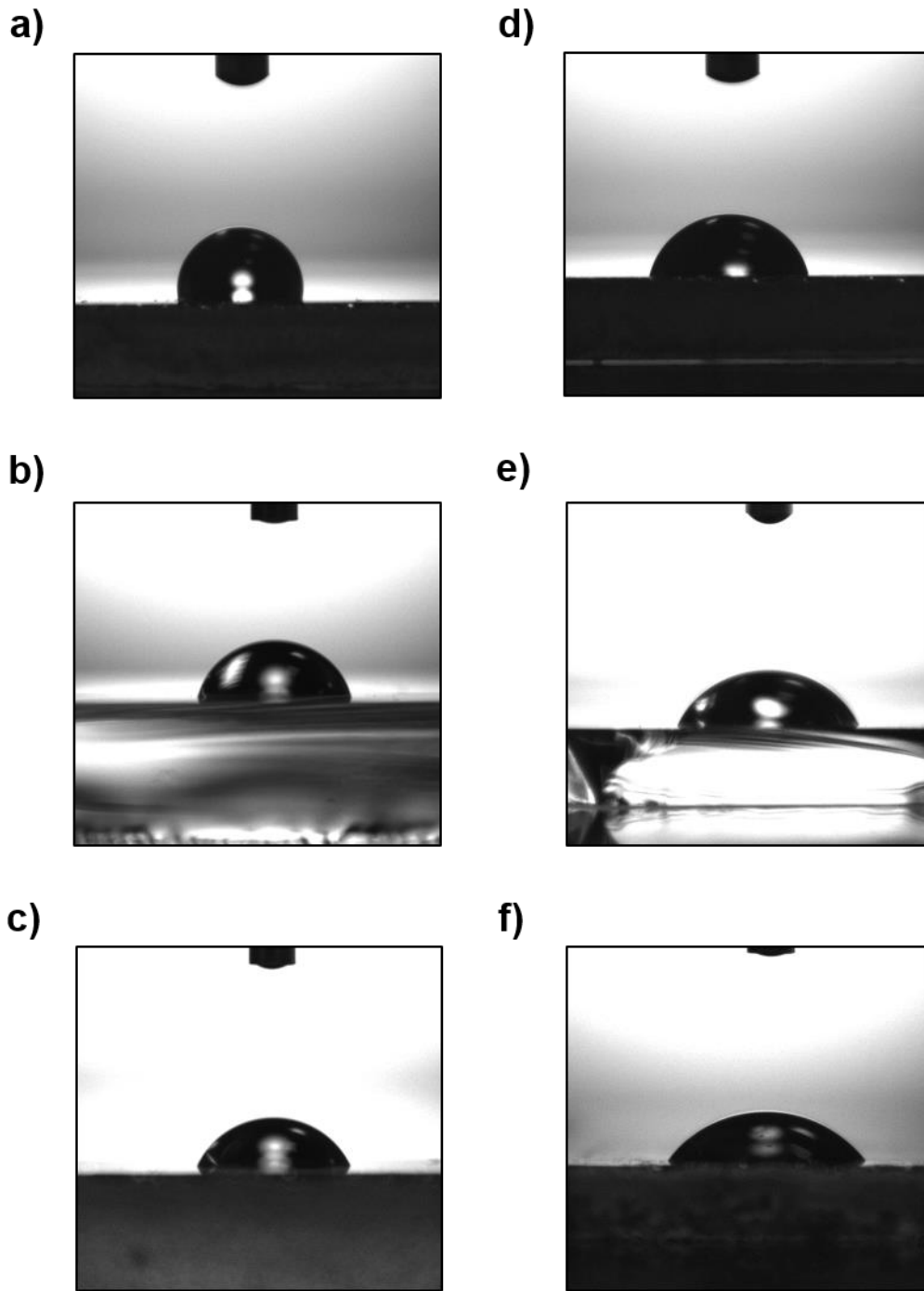


**Figure 20.** Images showing the contact angle formed between a drop water and the hematite film surface: a)  $\alpha\text{-Fe}_2\text{O}_3$  (500°C), b)  $\alpha\text{-Fe}_2\text{O}_3 + \text{Sn}^{4+}$  (500°C), c)  $\alpha\text{-Fe}_2\text{O}_3 + \text{Zn}^{2+}$  (500°C), d)  $\alpha\text{-Fe}_2\text{O}_3$  (800°C), e)  $\alpha\text{-Fe}_2\text{O}_3 + \text{Sn}^{4+}$  (800°C) and f)  $\alpha\text{-Fe}_2\text{O}_3 + \text{Zn}^{2+}$  (800°C).



**Table 7.** Roughness values and average contact angles for hematite films.

Film	Average contact angle	$R_q$ (nm)
$\alpha\text{-Fe}_2\text{O}_3$ (500°C)	160.26	6.47
$\alpha\text{-Fe}_2\text{O}_3 + \text{Sn}^{4+}$ (500°C)	80.56	4.87
$\alpha\text{-Fe}_2\text{O}_3 + \text{Zn}^{2+}$ (500°C)	67.95	5.76
$\alpha\text{-Fe}_2\text{O}_3$ (800°C)	78.80	15.35
$\alpha\text{-Fe}_2\text{O}_3 + \text{Sn}^{4+}$ (800°C)	66.86	8.66
$\alpha\text{-Fe}_2\text{O}_3 + \text{Zn}^{2+}$ (800°C)	53.92	11.64

Contact angles can be influenced by various parameters such as surface roughness, surface energy and surface cleanliness<sup>83</sup>. In this work the influence of the surface roughness on contact angles was investigated by using atomic force microscopy (Figure 21). Hematite films synthesized at 500°C exhibited a different surface appearance from that of films prepared at 800°C. The surface of 500°C-treated films was smooth while the 800°C-treated film surface was significantly rough. These results are in good agreement with the SEM results. In addition, the roughness was also assessed by the  $R_q$  value (RMS roughness) which is defined as the standard deviation of height values<sup>84</sup>:

$$R_q = \sqrt{\frac{\sum (Z_i - Z_m)^2}{N}} \quad (19)$$

where  $Z_i$  is a specific height value,  $Z_m$  is the average of all height values and  $N$  is the number of height values recorded. Table 7 shows the  $R_q$  values for hematite films. For films of the same composition (for example, undoped films prepared at 500°C and 800°C), the  $R_q$  values were higher for films synthesized at 800°C than those of films prepared at 500°C. These results are in accordance with the film roughness description based on the AFM micrographs (Figure 21) that showed that 800°C-treated films are rougher than 500°C-treated films. In relation to the films

prepared at the same temperature, the  $R_q$  values vary and the undoped films had the higher RMS roughness.

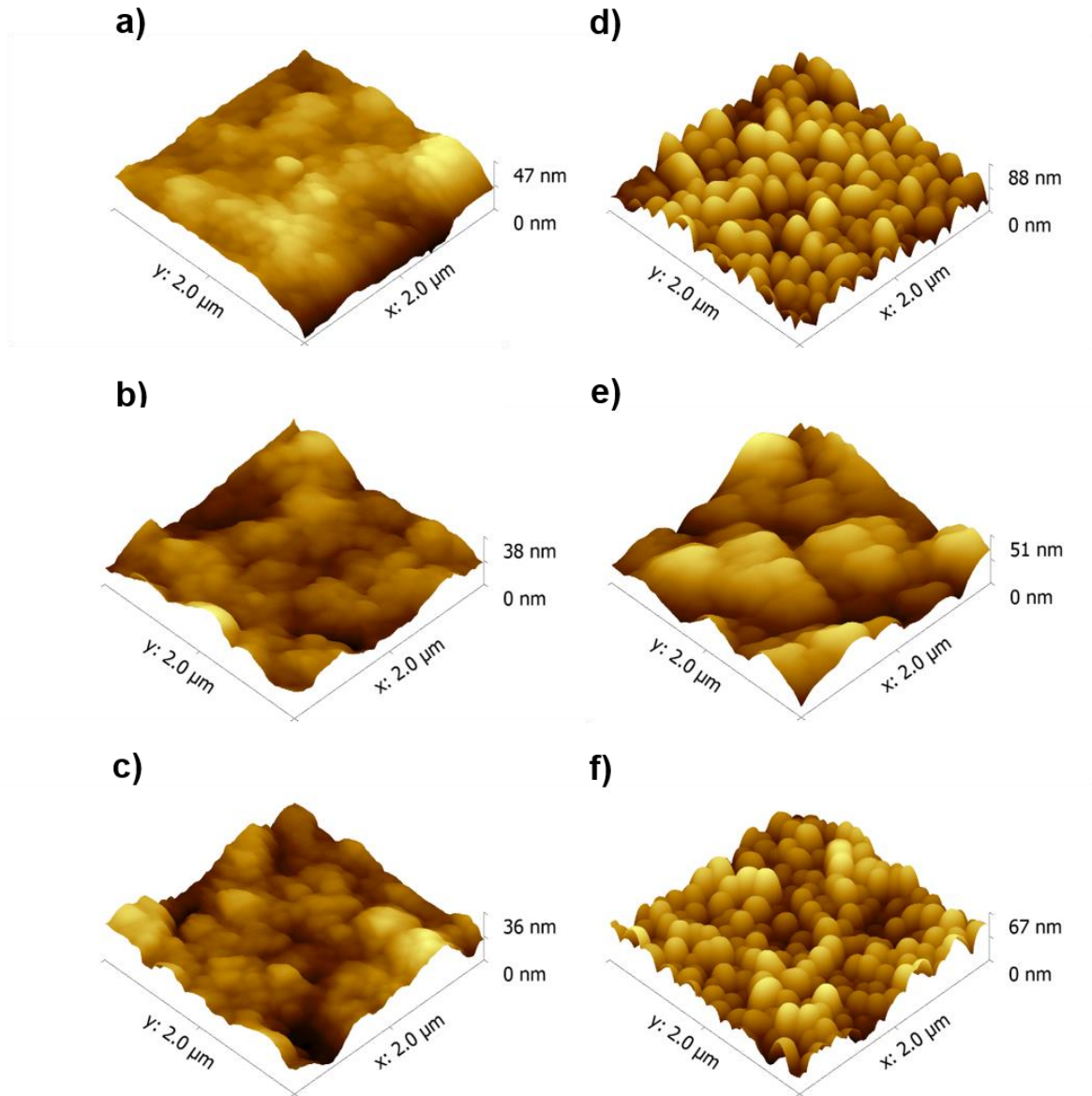


**Figure 21.** AFM micrographs: a)  $\alpha\text{-Fe}_2\text{O}_3$  (500°C), b)  $\alpha\text{-Fe}_2\text{O}_3 + \text{Sn}^{4+}$  (500°C), c)  $\alpha\text{-Fe}_2\text{O}_3 + \text{Zn}^{2+}$  (500°C), d)  $\alpha\text{-Fe}_2\text{O}_3$  (800°C), e)  $\alpha\text{-Fe}_2\text{O}_3 + \text{Sn}^{4+}$  (800°C) and f)  $\alpha\text{-Fe}_2\text{O}_3 + \text{Zn}^{2+}$  (800°C).

Therefore, results suggested that the surface roughness of hematite films has influenced their water affinity. The hematite films prepared at 800°C showed a better affinity for water because they had higher  $R_q$  values than those of films synthesized at 500°C.

## 6. GENERAL DISCUSSION

According to Figure 18, films treated at 500°C were unstable and exhibited the lowest photocurrent densities, whereas hematite films treated at 800°C were more stable and exhibited the highest photocurrent densities at 1.23 V<sub>RHE</sub>. The difference in the catalytic response (under sunlight illumination) of films thermally treated at different temperatures can be attributed to the differences in the roughness. According to Table 7, water covers a larger surface area when it interacts with films synthesized at 800°C instead of 500°C-treated films. AFM results suggested that the higher RMS roughness of 800°C-treated films contributed to their high wettability (lower contact angles). Another manner to explain the main differences in the catalytic activity of hematite films due to thermal treatment is by considering the surface area. As shown in Figure 14, the films that exhibited higher  $R_q$  values were composed of larger grains and were porous, while films prepared at 500°C had lower RMS roughness and consisted of smaller grains well packed. Thus, hematite films prepared at 800°C had more surface area for the OER than that of the hematite films prepared at 500°C.

The insertion of Sn<sup>4+</sup> or Zn<sup>2+</sup> affected differently the photocatalytic performance of hematite films synthesized at 500°C. The stability and photocurrent density exhibited by the undoped and Zn-modified film was very similar (Figure 18), with no significant improvement. A hypothesis is that the Zn<sup>2+</sup> impurities are acting as recombination sites favoring the increase in the recombination rate (electron-hole pairs), resulting in a poor efficiency of surface chemical reactions. According to the EIS and contact angle results, the Zn-modified film exhibited a higher N<sub>D</sub> value and the highest surface affinity with water (lowest final contact angle). Based on these results, a very good performance of Zn-modified hematite film was expected, however, the surface or bulk recombination sites played a major role in the photocatalytic response. This explanation is also complemented by the absorption spectra (Figure 15a), which showed that the insertion of Zn<sup>2+</sup> dopants did not enhance the absorbance in comparison with the undoped hematite film. On the other hand, the hematite film prepared with Sn<sup>4+</sup> impurities slightly improved its photocurrent density in comparison with the undoped hematite film (Figure 18). This can be attributed to the improvement on the absorbance intensity which suggests a lower recombination rate. It is worth to mention that Sn<sup>4+</sup> impurities influenced

differently on hematite films than the  $\text{Zn}^{2+}$  dopants. That means that the Sn-modified hematite film had the lowest overpotential ( $\eta_{\text{ox}} = 0.05$ ) while the Zn-modified hematite film had a higher overpotential ( $\eta_{\text{ox}} = 0.40$ ). In addition, the estimated  $N_b$  value of the Sn-modified hematite film suggested that  $\text{Sn}^{4+}$  is acting as acceptor rather than as a donor. Finally, since the improvement on the photocatalytic properties of pure hematite film was poor when the  $\text{Sn}^{4+}$  and  $\text{Zn}^{2+}$  dopants were introduced, it is probable that most of the impurities segregated. By using the PC method, Souza et al.<sup>49</sup> prepared hematite electrode doped with Si (0.5%) and Si (2.0%), in which they found that a certain concentration of Si segregated at the hematite grain boundaries. Additionally, they concluded that Si segregated at the grains hindered the photocatalytic activity of hematite (promoting the recombination rate of hole-electron pairs), and that was why the performance of the Si(2.0%)-modified hematite film was as poor as that of the pure hematite film, whereas the Si(0.5%)-modified hematite film had the highest photocurrent at 1.23 V<sub>RHE</sub>. It is also worth to mention that, since the segregation of the impurities causes the formation of unintentional composites, composites can also exhibit a better photocatalytic performance than that of the pure hematite electrode as demonstrated in the work of Shen et al.<sup>85</sup>. In that investigation, they prepared hematite nanorod electrodes doped with  $\text{W}^{6+}$  and modified with a thin layer of  $\text{WO}_3$  (composite). The results showed that  $\text{W}^{6+}$ -modified hematite films exhibited the best performance for water splitting, but the  $\text{WO}_3$ -modified  $\alpha\text{-Fe}_2\text{O}_3$  film also had a better photocurrent in comparison with the pure hematite film. However, because it was not observed a great improvement on the catalytic response of Sn and Zn-modified hematite films, it seems that the possible segregation of dopants does not enhance the hematite performance for the OER under illumination.

As mentioned in the above paragraph, the addition of the  $\text{Zn}^{2+}$  into the hematite structure did not result in a better performance of the hematite film prepared at 500°C. The explanation given was that  $\text{Zn}^{2+}$  is acting as a recombination site. Another explanation of the poor photocatalytic response of the Zn-modified hematite film must be related to the formation of ZnO on the hematite surface (segregation), which is soluble in a basic medium<sup>86</sup>. Indeed, cyclic voltammetry results of the Zn-modified hematite film (no shown here) performed at 20 cycles indicated that currents at cathodic potentials were unstable; thus, this may be related to the dissolution of the Zn-modified hematite material.

Unlike doped hematite films prepared at 500°C, not only the  $\text{Sn}^{4+}$  dopants but also the  $\text{Zn}^{2+}$  dopants enhanced the photocatalytic properties of hematite electrodes treated at 800°C. In addition, the relative increase in the photocurrent caused by the impurities (for films prepared at 800°C) was very similar to that observed by the Sn-modified hematite film treated at 500°C (Figure 18). Moreover, modified films prepared at 800°C were more stable than those prepared at 500°C. This suggests that  $\text{Sn}^{4+}$  and  $\text{Zn}^{2+}$  impurities were incorporated more efficiently into the hematite films at 800°C. According to the EIS results, an increase in the  $N_D$  values was found for the hematite films modified with  $\text{Sn}^{4+}$  and  $\text{Zn}^{2+}$ , which confirmed that  $\text{Sn}^{4+}$  and  $\text{Zn}^{2+}$  acted as donors. Another effect that has probably affected the properties of the 800°C-treated films is the unintentional doping with  $\text{Sn}^{4+}$  ions from the F- $\text{SnO}_2$  layer. According to literature, the migration of tin ions into hematite films is promoted at high sintering temperatures as 800°C<sup>46; 79</sup>, enhancing the photoelectrochemical performance of the hematite electrodes. Therefore, these results indicate that a better degree of incorporation of the dopants was achieved when films were synthesized at 800°C rather than at 500°.

Despite the higher photocurrent densities and good stability of the 800°C-treated hematite films, it is possible that  $\text{Zn}^{2+}$  and  $\text{Sn}^{4+}$  dopants also segregated since a great improvement on performance of the hematite electrodes was not achieved. SEM images suggested that dopants may have segregated at the hematite grain boundaries because the grain boundaries of the modified hematite films were smaller than those of the undoped films. The segregation of the dopants could have created a surface intermediate level (optical band gap analysis, Figure 16) which acted as recombination sites. Moreover, the Raman spectroscopy results (Figure 13) could have a relation with the segregation of dopants. Dopants segregated at the grain boundaries could have controlled the diffusion processes for the growth of hematite grains, and, thus, preventing more the formation of defects in the grains. Nevertheless, further investigation should be conducted in order to have a better understanding of the Raman spectra results.

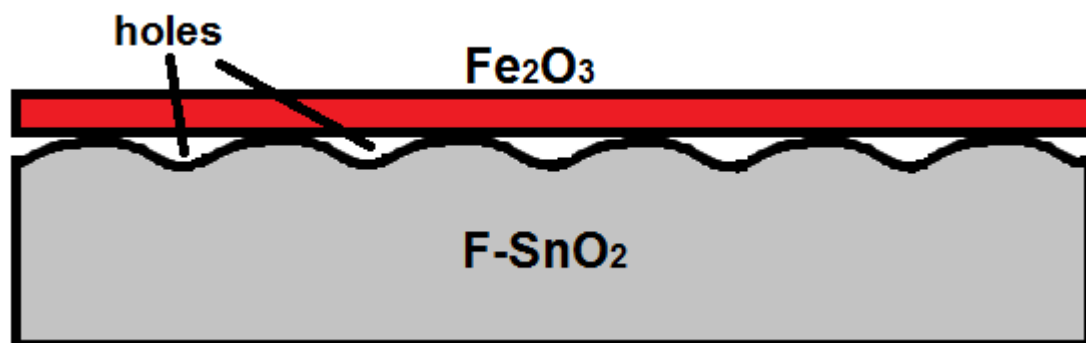


**Figure 22** Schematic representation of cross-section STEM images showing that the hematite films prepared by the PC method did not completely adhere to  $\text{F-SnO}_2$  surface. Adapted from ref. 84.

In general, the hematite films prepared by the polymerized complex method exhibited a low performance for the water oxidation. In a previous work that used this method<sup>87</sup>, the authors demonstrated that the poor catalytic response of hematite were related to the poor contact between hematite and  $\text{F-SnO}_2$  layer (transparent conductive glass substrate). According to the cross-section STEM images, only few points of the hematite film were in contact with the  $\text{F-SnO}_2$  layer. A schematic representation of the STEM images obtained by the authors is shown in Figure 22. Therefore, not all the photogenerated electrons are harvested resulting in a low photocurrent density. Consequently, it is believed that the hematite films synthesized in this work were not well deposited on the  $\text{F-SnO}_2$  film, which may have affected the performance of the undoped and modified hematite films.

## 7. CONCLUSIONS

Undoped hematite films and hematite films modified with  $\text{Sn}^{4+}$  and  $\text{Zn}^{2+}$  were prepared by using the Polymerized Complex method and at two different temperatures ( $500^\circ\text{C}$  and  $800^\circ\text{C}$ ). The thickness of the  $500^\circ\text{C}$ -treated hematite films was about 162 nm, whereas the thickness of the  $800^\circ\text{C}$ -treated hematite was approximately 285 nm. Moreover, the results showed that this method permits to prepared thin films of hematite with the (001) plane oriented perpendicular to the substrate. Hematite electrodes prepared at  $800^\circ\text{C}$  exhibited the best stability and photocurrents. Thus, the photocatalytic properties of hematite films were influenced by the heat treatment temperature. The better performance of the  $800^\circ\text{C}$ -treated hematite films was attributed to their higher roughness as corroborated by AFM and

contact angle measurements. In relation with effect of the dopants, linear sweep voltammetry results and impedance analysis showed that  $\text{Sn}^{4+}$  and  $\text{Zn}^{2+}$  dopants affected differently on the experimental onset potential for the OER both in the dark and under illumination. Moreover, impurities also slightly improved the performance of the hematite electrodes with the exception of the Zn-modified hematite film synthesized at  $500^{\circ}\text{C}$ . Furthermore, the  $\text{Sn}^{4+}$  and  $\text{Zn}^{2+}$  dopants were incorporated into  $800^{\circ}\text{C}$ -treated hematite electrodes more efficiently than those of the  $500^{\circ}\text{C}$ -treated hematite films. Although EIS results demonstrated that dopants were incorporated into the hematite structure both at  $500^{\circ}\text{C}$  and  $800^{\circ}\text{C}$ , it is probable that most of the dopants segregated acting as recombination sites that negatively affected the photocatalytic properties. Regardless of the dopant segregation, both undoped and modified hematite films exhibited a low performance for the OER under illumination conditions. The most plausible explanation can be the poor contact between the hematite and FTO layer which severely worsened its catalytic response.

## **8. SUGGESTIONS FOR FUTURE WORK**

The performance of hematite films prepared by the PC method can still be improved in different ways. One important topic of investigation would be the improvement of the interface between the hematite and the FTO layer. This problem of the poor contact can be overcome if, before the deposition of hematite by the PC method, a thin hematite layer prepared by another technique (that does not have problems with the poor contact) is deposited. Thus, several chemical and physical methods for preparing thin layer of oxides can be used: hydrothermal methodology, Atomic Layer Deposition (ALD), Chemical Vapor Deposition (CVD). Another way to improve the contact between the hematite and the FTO layer is by treating the FTO layer before the hematite film depositions. It is possible that the roughness of the FTO is preventing getting a good contact between the hematite and the FTO layer, therefore, reducing the roughness of the FTO layer by using a plasma treatment is a good approach to the contact problem.

## 9. REFERENCES

- 1 SOLANGI, K. H. et al. A review on global solar energy policy. **Renewable and Sustainable Energy Reviews**, v. 15, n. 4, p. 2149-2163, 2011. ISSN 1364-0321. Disponível em: < <http://www.sciencedirect.com/science/article/pii/S1364032111000220> >.
- 2 AGENCY, I. E. **Key World Energy Statistics**: 80 p. 2013.
- 3 LIAO, C.-H.; HUANG, C.-W.; WU, J. C. S. Hydrogen Production from Semiconductor-based Photocatalysis via Water Splitting. **Catalysts**, v. 2, n. 4, p. 490-516, 2012. ISSN 2073-4344. Disponível em: < <http://www.mdpi.com/2073-4344/2/4/490> >.
- 4 KOUMI NGOH, S.; NJOMO, D. An overview of hydrogen gas production from solar energy. **Renewable and Sustainable Energy Reviews**, v. 16, n. 9, p. 6782-6792, 2012. ISSN 1364-0321. Disponível em: < <http://www.sciencedirect.com/science/article/pii/S1364032112004698> >.
- 5 SEQUEIRA, C. A. C.; SANTOS, D. M. F. Hydrogen production. **Ciência & Tecnologia dos Materiais**, v. 22, p. 76-86, 2010. ISSN 0870-8312. Disponível em: < [http://www.scielo.gpeari.mctes.pt/scielo.php?script=sci\\_arttext&pid=S0870-83122010000200013&nrm=iso](http://www.scielo.gpeari.mctes.pt/scielo.php?script=sci_arttext&pid=S0870-83122010000200013&nrm=iso) >.
- 6 WANG, Z. et al. Comparison of thermochemical, electrolytic, photoelectrolytic and photochemical solar-to-hydrogen production technologies. **International Journal of Hydrogen Energy**, v. 37, n. 21, p. 16287-16301, 2012. ISSN 0360-3199. Disponível em: < <http://www.sciencedirect.com/science/article/pii/S0360319912007033> >.
- 7 DINCER, I. Green methods for hydrogen production. **International Journal of Hydrogen Energy**, v. 37, n. 2, p. 1954-1971, 2012. ISSN 0360-3199. Disponível em: < <http://www.sciencedirect.com/science/article/pii/S0360319911019823> >.
- 8 JOSHI, A. S.; DINCER, I.; REDDY, B. V. Solar hydrogen production: A comparative performance assessment. **International Journal of Hydrogen Energy**, v. 36, n. 17, p. 11246-11257, 2011. ISSN 0360-3199. Disponível em: < <http://www.sciencedirect.com/science/article/pii/S0360319910023372> >.



- 9 BARD, A.; FAULKNER, L. **Electrochemical Methods: Fundamentals and Applications**. John Wiley & Sons, Inc, 2001. ISBN 978-0-471-04372-0. Disponível em: < <http://www.wiley.com/WileyCDA/WileyTitle/productCd-0471043729.html> >.
- 10 SATO, N. **Electrochemistry at Metal and Semiconductor Electrodes**. Amsterdam: Elsevier Science, 1998. ISBN 9780444828084.
- 11 SCHMICKLER, W.; SANTOS, E. **Interfacial Electrochemistry**. 2nd edition. Springer, 2010.
- 12 KRISHNAN, R. Fundamentals of Semiconductor Electrochemistry and Photoelectrochemistry. In: (Ed.). **Encyclopedia of Electrochemistry**: Wiley-VCH Verlag GmbH & Co. KGaA, 2007. ISBN 9783527610426.
- 13 ROEL VAN DE, K.; MICHAEL, G. **Photoelectrochemical Hydrogen Production** 2012.
- 14 MEMMING, R. In: (Ed.). **Semiconductor Electrochemistry**: Wiley-VCH Verlag GmbH, 2007. ISBN 9783527613069.
- 15 VAN DE KROL, R.; LIANG, Y.; SCHOONMAN, J. Solar hydrogen production with nanostructured metal oxides. **Journal of Materials Chemistry**, v. 18, n. 20, p. 2311-2320, 2008. ISSN 0959-9428. Disponível em: < <http://dx.doi.org/10.1039/B718969A> >.
- 16 FAN, Y. et al. An overview on water splitting photocatalysts. **Frontiers of Chemistry in China**, v. 4, n. 4, p. 343-351, 2009/12/01 2009. ISSN 1673-3495. Disponível em: < <http://dx.doi.org/10.1007/s11458-009-0100-1> >.
- 17 LOPES, T. et al. Characterization of photoelectrochemical cells for water splitting by electrochemical impedance spectroscopy. **International Journal of Hydrogen Energy**, v. 35, n. 20, p. 11601-11608, 2010. ISSN 0360-3199. Disponível em: < <http://www.sciencedirect.com/science/article/pii/S0360319910006622> >.
- 18 NOWOTNY, J. **Oxide Semiconductors for Solar Energy Conversion: Titanium Dioxide**. Florida: CRC Press, 2012.
- 19 **Metal Oxides: Chemistry and Applications**. Florida: Taylor & Francis Group, 2006.

- 20 CHIANG, Y.-M.; BIRNIE III, D.; KINGERY, D. W. **Physical Ceramics: Principles for Ceramics Science and Engineering**. New York: John Wiley & Sons, 1997.
- 21 XU, C. X. et al. Photoluminescent properties of copper-doped zinc oxide nanowires. **Nanotechnology**, v. 15, n. 7, p. 856, 2004. ISSN 0957-4484. Disponível em: < <http://stacks.iop.org/0957-4484/15/i=7/a=026> >.
- 22 XAVIER, A. M.; FERREIRA, F. F.; SOUZA, F. L. Morphological and structural evolution from akaganeite to hematite of nanorods monitored by ex situ synchrotron X-ray powder diffraction. **RSC Advances**, v. 4, n. 34, p. 17753-17759, 2014. Disponível em: < <http://dx.doi.org/10.1039/C3RA42753F> >.
- 23 LIAO, P.; TOROKER, M. C.; CARTER, E. A. Electron Transport in Pure and Doped Hematite. **Nano Letters**, v. 11, n. 4, p. 1775-1781, 2011/04/13 2011. ISSN 1530-6984. Disponível em: < <http://dx.doi.org/10.1021/nl200356n> >. Acesso em: 2014/08/12.
- 24 SIVULA, K.; LE FORMAL, F.; GRÄTZEL, M. Cover Picture: Solar Water Splitting: Progress Using Hematite ( $\alpha$ -Fe<sub>2</sub>O<sub>3</sub>) Photoelectrodes (ChemSusChem 4/2011). **ChemSusChem**, v. 4, n. 4, p. 417-417, 2011. ISSN 1864-564X. Disponível em: < <http://dx.doi.org/10.1002/cssc.201190014> >.
- 25 ROLLMANN, G. et al. First-principles calculation of the structure and magnetic phases of hematite. **Physical Review B**, v. 69, n. 16, p. 165107, 2004. Disponível em: < <http://link.aps.org/doi/10.1103/PhysRevB.69.165107> >.
- 26 LEE, M. H. et al. Nanostructured Ti-doped hematite ( $\alpha$ -Fe<sub>2</sub>O<sub>3</sub>) photoanodes for efficient photoelectrochemical water oxidation. **International Journal of Hydrogen Energy**, n. 0, ISSN 0360-3199. Disponível em: < <http://www.sciencedirect.com/science/article/pii/S0360319913024622> >.
- 27 WANG, L. et al. Enhancing the Water Splitting Efficiency of Sn-Doped Hematite Nanoflakes by Flame Annealing. **Chemistry – A European Journal**, v. 20, n. 1, p. 77-82, 2014. ISSN 1521-3765. Disponível em: < <http://dx.doi.org/10.1002/chem.201303427> >.
- 28 LEE, C.-Y. et al. Si-doped Fe<sub>2</sub>O<sub>3</sub> nanotubular/nanoporous layers for enhanced photoelectrochemical water splitting. **Electrochemistry Communications**, v. 34, n. 0, p. 308-311, 2013. ISSN 1388-2481. Disponível em: < <http://www.sciencedirect.com/science/article/pii/S138824811300283X> >.

- 29 KUMARI, S. et al. Enhanced Photoelectrochemical Response of Zn-Dotted Hematite. **International Journal of Photoenergy**, v. 2007, p. 6, 2007. Disponível em: < <http://dx.doi.org/10.1155/2007/87467> >.
- 30 LIU, Y.; YU, Y.-X.; ZHANG, W.-D. Photoelectrochemical properties of Ni-doped Fe<sub>2</sub>O<sub>3</sub> thin films prepared by electrodeposition. **Electrochimica Acta**, v. 59, n. 0, p. 121-127, 2012. ISSN 0013-4686. Disponível em: < <http://www.sciencedirect.com/science/article/pii/S0013468611015829> >.
- 31 DE CARVALHO, V. A. N. et al. Highly oriented hematite nanorods arrays for photoelectrochemical water splitting. **Journal of Power Sources**, v. 205, n. 0, p. 525-529, 2012. ISSN 0378-7753. Disponível em: < <http://www.sciencedirect.com/science/article/pii/S0378775312001929> >.
- 32 CHA, H. G. et al. Facile preparation of Fe<sub>2</sub>O<sub>3</sub> thin film with photoelectrochemical properties. **Chemical Communications**, v. 47, n. 8, p. 2441-2443, 2011. ISSN 1359-7345. Disponível em: < <http://dx.doi.org/10.1039/C0CC04775A> >.
- 33 KUMAR, P. et al. Electrodeposited zirconium-doped  $\alpha$ -Fe<sub>2</sub>O<sub>3</sub> thin film for photoelectrochemical water splitting. **International Journal of Hydrogen Energy**, v. 36, n. 4, p. 2777-2784, 2011. ISSN 0360-3199. Disponível em: < <http://www.sciencedirect.com/science/article/pii/S0360319910023220> >.
- 34 SINGH, A. P. et al. Photoelectrochemical properties of hematite films grown by plasma enhanced chemical vapor deposition. **International Journal of Hydrogen Energy**, v. 37, n. 19, p. 13983-13988, 2012. ISSN 0360-3199. Disponível em: < <http://www.sciencedirect.com/science/article/pii/S0360319912015157> >.
- 35 LIN, Y. et al. Nanonet-Based Hematite Heteronanostructures for Efficient Solar Water Splitting. **Journal of the American Chemical Society**, v. 133, n. 8, p. 2398-2401, 2011/03/02 2011. ISSN 0002-7863. Disponível em: < <http://dx.doi.org/10.1021/ja110741z> >. Acesso em: 2014/09/12.
- 36 KUMARI, S. et al. Spray pyrolytically deposited nanoporous Ti<sup>4+</sup> doped hematite thin films for efficient photoelectrochemical splitting of water. **International Journal of Hydrogen Energy**, v. 35, n. 9, p. 3985-3990, 2010. ISSN 0360-3199. Disponível em: < <http://www.sciencedirect.com/science/article/pii/S0360319910001989> >.
- 37 MEMAR, A. et al. Study on photocurrent of bilayers photoanodes using different combination of WO<sub>3</sub> and Fe<sub>2</sub>O<sub>3</sub>. **Solar Energy**, v. 84, n. 8, p. 1538-

- 1544, 2010. ISSN 0038-092X. Disponível em: < <http://www.sciencedirect.com/science/article/pii/S0038092X10002070> >.
- 38 MIYAKE, H.; KOZUKA, H. Photoelectrochemical Properties of Fe<sub>2</sub>O<sub>3</sub>-Nb<sub>2</sub>O<sub>5</sub> Films Prepared by Sol-Gel Method. **The Journal of Physical Chemistry B**, v. 109, n. 38, p. 17951-17956, 2005/09/01 2005. ISSN 1520-6106. Disponível em: < <http://dx.doi.org/10.1021/jp058051b> >. Acesso em: 2014/09/12.
- 39 DURÃES, L. et al. Characterization of iron(III) oxide/hydroxide nanostructured materials produced by sol-gel technology based on the Fe(NO<sub>3</sub>)<sub>3</sub>·9H<sub>2</sub>O-C<sub>2</sub>H<sub>5</sub>OH-CH<sub>3</sub>CHCH<sub>2</sub>O system. **Materials Chemistry and Physics**, v. 130, n. 1-2, p. 548-560, 2011. ISSN 0254-0584. Disponível em: < <http://www.sciencedirect.com/science/article/pii/S0254058411006171> >.
- 40 ZNAIDI, L. Sol-gel-deposited ZnO thin films: A review. **Materials Science and Engineering: B**, v. 174, n. 1-3, p. 18-30, 2010. ISSN 0921-5107. Disponível em: < <http://www.sciencedirect.com/science/article/pii/S0921510710004630> >.
- 41 KAKIHANA, M. Invited review "sol-gel" preparation of high temperature superconducting oxides. **Journal of Sol-Gel Science and Technology**, v. 6, n. 1, p. 7-55, 1996/01/01 1996. ISSN 0928-0707. Disponível em: < <http://dx.doi.org/10.1007/BF00402588> >.
- 42 NIEDERBERGER, M.; PINNA, N. **Metal Oxide Nanoparticles in Organic Solvents**. Springer London, 2009.
- 43 PIERRE, J. L.; GAUTIER-LUNEAU, I. Iron and citric acid: A fuzzy chemistry of ubiquitous biological relevance. **Biometals**, v. 13, n. 1, p. 91-96, 2000/03/01 2000. ISSN 0966-0844. Disponível em: < <http://dx.doi.org/10.1023/A%3A1009225701332> >.
- 44 SILVA, A. M. N. et al. Iron(iii) citrate speciation in aqueous solution. **Dalton Transactions**, n. 40, p. 8616-8625, 2009. ISSN 1477-9226. Disponível em: < <http://dx.doi.org/10.1039/B910970F> >.
- 45 WU, Y.; WANG, X. Preparation and characterization of single-phase  $\alpha$ -Fe<sub>2</sub>O<sub>3</sub> nano-powders by Pechini sol-gel method. **Materials Letters**, v. 65, n. 13, p. 2062-2065, 2011. ISSN 0167-577X. Disponível em: < <http://www.sciencedirect.com/science/article/pii/S0167577X11003703> >.

- 46 SIVULA, K. et al. Photoelectrochemical Water Splitting with Mesoporous Hematite Prepared by a Solution-Based Colloidal Approach. **Journal of the American Chemical Society**, v. 132, n. 21, p. 7436-7444, 2010/06/02 2010. ISSN 0002-7863. Disponível em: < <http://dx.doi.org/10.1021/ja101564f> >.
- 47 CARVALHO JUNIOR, W. M. D. **Propriedades fotocatalíticas de filmes nanoestruturados de óxido de ferro sintetizados pelo método hidrotérmico**. 2013. (Mestrado ). Nanociências e Materiais Avançados, Universidade Federal do ABC, São Paulo.
- 48 ITO, N. M. **Estudo das propriedades físico-químicas de nanoestruturas de óxido de ferro para aplicações fotocatalíticas**. 2013. (Mestrado). Nanociências e Materiais Avançados, Universidade Federal do ABC, São Paulo.
- 49 SOUZA, F. L. et al. Nanostructured hematite thin films produced by spin-coating deposition solution: Application in water splitting. **Solar Energy Materials and Solar Cells**, v. 93, n. 3, p. 362-368, 2009. ISSN 0927-0248. Disponível em: < <http://www.sciencedirect.com/science/article/pii/S0927024808004479> >.
- 50 RAMOS DE LIMA, B. H. **Análise estrutural de filmes finos de hematite produzidos por *spin-coating* para geração de hidrogênio**. 2010. (Mestre). Ciência e Engenharia de Materiais, Universidade Federal de São Carlos., São Carlos, São Paulo.
- 51 SHANNON, R. Revised effective ionic radii and systematic studies of interatomic distances in halides and chalcogenides. **Acta Crystallographica Section A**, v. 32, n. 5, p. 751-767, 1976. ISSN 0567-7394. Disponível em: < <http://dx.doi.org/10.1107/S0567739476001551> >.
- 52 UCHIYAMA, H.; YUKIZAWA, M.; KOZUKA, H. Photoelectrochemical Properties of Fe<sub>2</sub>O<sub>3</sub>-SnO<sub>2</sub> Films Prepared by Sol-Gel Method. **The Journal of Physical Chemistry C**, v. 115, n. 14, p. 7050-7055, 2011/04/14 2011. ISSN 1932-7447. Disponível em: < <http://dx.doi.org/10.1021/jp112279k> >. Acesso em: 2014/09/05.
- 53 AMI, T.; SUZUKI, M. MOCVD growth of (100)-oriented CeO<sub>2</sub> thin films on hydrogen-terminated Si(100) substrates. **Materials Science and Engineering: B**, v. 54, n. 1-2, p. 84-91, 1998. ISSN 0921-5107. Disponível em: < <http://www.sciencedirect.com/science/article/pii/S0921510798001330> >.

- 54 KAY, A.; CESAR, I.; GRÄTZEL, M. New Benchmark for Water Photooxidation by Nanostructured  $\alpha$ -Fe<sub>2</sub>O<sub>3</sub> Films. **Journal of the American Chemical Society**, v. 128, n. 49, p. 15714-15721, 2006/12/01 2006. ISSN 0002-7863. Disponível em: < <http://dx.doi.org/10.1021/ja064380l> >. Acesso em: 2014/09/05.
- 55 MONSHI, A.; FOROUGHI, M.; MONSHI, M. Modified Sherrer Equation to Estimate More Accurately Nano-Crystallite Size Using XRD. **World Journal of Nano Science and Engineering**, v. 2, 2012.
- 56 LANGFORD, J. I.; WILSON, A. J. C. Scherrer after sixty years: A survey and some new results in the determination of crystallite size. **Journal of Applied Crystallography**, v. 11, n. 2, p. 102-113, 1978. ISSN 1600-5767. Disponível em: < <http://dx.doi.org/10.1107/S0021889878012844> >.
- 57 JUBB, A. M.; ALLEN, H. C. Vibrational Spectroscopic Characterization of Hematite, Maghemite, and Magnetite Thin Films Produced by Vapor Deposition. **ACS Applied Materials & Interfaces**, v. 2, n. 10, p. 2804-2812, 2010/10/27 2010. ISSN 1944-8244. Disponível em: < <http://dx.doi.org/10.1021/am1004943> >.
- 58 MIESSLER, G. L.; TARR, D. A. **Inorganic Chemistry**. 3rd edition. Prentice Hall, 2003. 720
- 59 FERRARO, J. R.; NAKAMOTO, K.; BROWN, C. W. **Introductory Raman Spectroscopy**. 2nd edition. San Diego: Elsevier, 2003.
- 60 CESAR, I. et al. Influence of Feature Size, Film Thickness, and Silicon Doping on the Performance of Nanostructured Hematite Photoanodes for Solar Water Splitting. **The Journal of Physical Chemistry C**, v. 113, n. 2, p. 772-782, 2009/01/15 2009. ISSN 1932-7447. Disponível em: < <http://dx.doi.org/10.1021/jp809060p> >.
- 61 YOGI, A.; VARSHNEY, D. Magnetic and structural properties of pure and Cr-doped haematite:  $\alpha$ -Fe<sub>2-x</sub>Cr<sub>x</sub>O<sub>3</sub> ( $0 \leq x \leq 1$ ). **Journal of Advanced Ceramics**, v. 2, n. 4, p. 360-369, 2013/12/01 2013. ISSN 2226-4108. Disponível em: < <http://dx.doi.org/10.1007/s40145-013-0084-7> >.
- 62 HU, Y.-S. et al. Pt-Doped  $\alpha$ -Fe<sub>2</sub>O<sub>3</sub> Thin Films Active for Photoelectrochemical Water Splitting. **Chemistry of Materials**, v. 20, n. 12, p. 3803-3805, 2008/06/01 2008. ISSN 0897-4756. Disponível em: < <http://dx.doi.org/10.1021/cm800144q> >.

- 63 SAREMI-YARAHMADI, S. et al. Nanostructured  $\alpha$ -Fe<sub>2</sub>O<sub>3</sub> Electrodes for Solar Driven Water Splitting: Effect of Doping Agents on Preparation and Performance. **The Journal of Physical Chemistry C**, v. 113, n. 12, p. 4768-4778, 2009/03/26 2009. ISSN 1932-7447. Disponível em: < <http://dx.doi.org/10.1021/jp808453z> >.
- 64 HAMANN, T. W. Splitting water with rust: hematite photoelectrochemistry. **Dalton Transactions**, v. 41, n. 26, p. 7830-7834, 2012. ISSN 1477-9226. Disponível em: < <http://dx.doi.org/10.1039/C2DT30340J> >.
- 65 ANPO, M.; TAKEUCHI, M. The design and development of highly reactive titanium oxide photocatalysts operating under visible light irradiation. **Journal of Catalysis**, v. 216, n. 1–2, p. 505-516, 2003. ISSN 0021-9517. Disponível em: < <http://www.sciencedirect.com/science/article/pii/S0021951702001045> >. Acesso em: 2003/6//.
- 66 PAN, X. et al. Defective TiO<sub>2</sub> with oxygen vacancies: synthesis, properties and photocatalytic applications. **Nanoscale**, v. 5, n. 9, p. 3601-3614, 2013. ISSN 2040-3364. Disponível em: < <http://dx.doi.org/10.1039/C3NR00476G> >.
- 67 VAN DE KROL, R.; GRATZEL, M. **Photoelectrochemical Hydrogen Production**. Springer Science 2012. 332
- 68 AYDIN, C. et al. Structural and optical characterization of sol–gel derived boron doped Fe<sub>2</sub>O<sub>3</sub> nanostructured films. **Journal of Sol-Gel Science and Technology**, v. 62, n. 3, p. 397-403, 2012/06/01 2012. ISSN 0928-0707. Disponível em: < <http://dx.doi.org/10.1007/s10971-012-2740-8> >.
- 69 AL-KUHAILI, M. F.; SALEEM, M.; DURRANI, S. M. A. Optical properties of iron oxide ( $\alpha$ -Fe<sub>2</sub>O<sub>3</sub>) thin films deposited by the reactive evaporation of iron. **Journal of Alloys and Compounds**, v. 521, n. 0, p. 178-182, 2012. ISSN 0925-8388. Disponível em: < <http://www.sciencedirect.com/science/article/pii/S0925838812001879> >.
- 70 SOUZA, F. L. et al. The influence of the film thickness of nanostructured [small alpha]-Fe<sub>2</sub>O<sub>3</sub> on water photooxidation. **Physical Chemistry Chemical Physics**, v. 11, n. 8, p. 1215-1219, 2009. ISSN 1463-9076. Disponível em: < <http://dx.doi.org/10.1039/B811946E> >.
- 71 LIAN, X. et al. Enhanced photoelectrochemical performance of Ti-doped hematite thin films prepared by the sol–gel method. **Applied Surface Science**, v. 258, n. 7, p. 2307-2311, 2012. ISSN 0169-4332. Disponível em: < <http://www.sciencedirect.com/science/article/pii/S016943321101556X> >.

- <sup>72</sup> ZANDI, O.; HAMANN, T. W. Enhanced Water Splitting Efficiency Through Selective Surface State Removal. **The Journal of Physical Chemistry Letters**, v. 5, n. 9, p. 1522-1526, 2014/05/01 2014. ISSN 1948-7185. Disponível em: < <http://dx.doi.org/10.1021/jz500535a> >.
- <sup>73</sup> LING, Y. et al. Sn-Doped Hematite Nanostructures for Photoelectrochemical Water Splitting. **Nano Letters**, v. 11, n. 5, p. 2119-2125, 2011/05/11 2011. ISSN 1530-6984. Disponível em: < <http://dx.doi.org/10.1021/nl200708y> >. Acesso em: 2014/10/29.
- <sup>74</sup> JIANG, R.; CHEN, C.; ZHENG, S. The non-linear fitting method to analyze the measured M–S plots of bipolar passive films. **Electrochimica Acta**, v. 55, n. 7, p. 2498-2504, 2010. ISSN 0013-4686. Disponível em: < <http://www.sciencedirect.com/science/article/pii/S001346860901473X> >.
- <sup>75</sup> LE FORMAL, F. et al. Passivating surface states on water splitting hematite photoanodes with alumina overlayers. **Chemical Science**, v. 2, n. 4, p. 737-743, 2011. ISSN 2041-6520. Disponível em: < <http://dx.doi.org/10.1039/C0SC00578A> >.
- <sup>76</sup> CARDON, F.; GOMES, W. P. On the determination of the flat-band potential of a semiconductor in contact with a metal or an electrolyte from the Mott-Schottky plot. **Journal of Physics D: Applied Physics**, v. 11, n. 4, p. L63, 1978. ISSN 0022-3727. Disponível em: < <http://stacks.iop.org/0022-3727/11/i=4/a=003> >.
- <sup>77</sup> LEDUC, J.; AHMED, S. M. Photoelectrochemical and impedance characteristics of specular hematite. 2. Deep bulk traps in specular hematite at small a.c. frequencies. **The Journal of Physical Chemistry**, v. 92, n. 23, p. 6661-6665, 1988/11/01 1988. ISSN 0022-3654. Disponível em: < <http://dx.doi.org/10.1021/j100334a034> >. Acesso em: 2014/09/14.
- <sup>78</sup> HOROWITZ, G. Capacitance-voltage measurements and flat-band potential determination on Zr-doped  $\alpha$ -Fe<sub>2</sub>O<sub>3</sub> single-crystal electrodes. **Journal of Electroanalytical Chemistry and Interfacial Electrochemistry**, v. 159, n. 2, p. 421-436, 1983. ISSN 0022-0728. Disponível em: < <http://www.sciencedirect.com/science/article/pii/S002207288380638X> >.
- <sup>79</sup> MIRBAGHERI, N. et al. Visible Light Driven Photoelectrochemical Water Oxidation by Zn- and Ti-Doped Hematite Nanostructures. **ACS Catalysis**, v. 4, n. 6, p. 2006-2015, 2014/06/06 2014. ISSN 2155-5435 2155-5435. Disponível em: < <http://dx.doi.org/10.1021/cs500372v> >. Acesso em: 2014/08/03.



- 80 FU, Z. et al. Highly photoactive Ti-doped  $\alpha$ -Fe<sub>2</sub>O<sub>3</sub> nanorod arrays photoanode prepared by a hydrothermal method for photoelectrochemical water splitting. **Electrochimica Acta**, v. 129, n. 0, p. 358-363, 2014. ISSN 0013-4686. Disponível em: < <http://www.sciencedirect.com/science/article/pii/S0013468614004630> >.
- 81 CAO, D. et al. A transparent Ti<sup>4+</sup> doped hematite photoanode protectively grown by a facile hydrothermal method. **CrystEngComm**, v. 15, n. 13, p. 2386-2391, 2013. Disponível em: < <http://dx.doi.org/10.1039/C3CE26811J> >.
- 82 SIVULA, K. Metal Oxide Photoelectrodes for Solar Fuel Production, Surface Traps, and Catalysis. **The Journal of Physical Chemistry Letters**, v. 4, n. 10, p. 1624-1633, 2013/05/16 2013. ISSN 1948-7185. Disponível em: < <http://dx.doi.org/10.1021/jz4002983> >. Acesso em: 2014/10/29.
- 83 BHUSHAN, B.; CHAE JUNG, Y.; NOSONOVSKY, M. Lotus Effect: Surfaces with Roughness-Induced Superhydrophobicity, Self-Cleaning, and Low Adhesion. In: BHUSHAN, B. (Ed.). **Springer Handbook of Nanotechnology**. 3rd: Springer-Verlag Berlin Heidelberg, 2010. ISBN 978-3-642-02524-2.
- 84 MILLER, J. D. et al. Effect of roughness as determined by atomic force microscopy on the wetting properties of PTFE thin films. **Polymer Engineering & Science**, v. 36, n. 14, p. 1849-1855, 1996. ISSN 1548-2634. Disponível em: < <http://dx.doi.org/10.1002/pen.10580> >.
- 85 SHEN, S. et al. Surface tuning for promoted charge transfer in hematite nanorod arrays as water-splitting photoanodes. **Nano Research**, v. 5, n. 5, p. 327-336, 2012/05/01 2012. ISSN 1998-0124. Disponível em: < <http://dx.doi.org/10.1007/s12274-012-0213-6> >.
- 86 MCDONALD, K. J.; CHOI, K.-S. Synthesis and Photoelectrochemical Properties of Fe<sub>2</sub>O<sub>3</sub>/ZnFe<sub>2</sub>O<sub>4</sub> Composite Photoanodes for Use in Solar Water Oxidation. **Chemistry of Materials**, v. 23, n. 21, p. 4863-4869, 2011/11/08 2011. ISSN 0897-4756. Disponível em: < <http://dx.doi.org/10.1021/cm202399g> >.
- 87 DE SOUZA, F. L. et al. Facile Routes to Produce Hematite Film for Hydrogen Generation from Photoelectro-Chemical Water Splitting. In: DE SOUZA, F. L. e LEITE, E. R. (Ed.). **Nanoenergy: Nanotechnology Applied for Energy Production**: Springer-Verlag Berlin Heidelberg, 2013.